

1 **Marine terraces of the last interglacial period along the Pacific** 2 **coast of South America (1°N-40°S)**

3 Roland Freisleben¹, Julius Jara-Muñoz¹, Daniel Melnick^{2,3}, José Miguel Martínez^{2,3}, Manfred R.
4 Strecker¹

5 ¹ Institut für Geowissenschaften, Universität Potsdam, 14476 Potsdam, Germany

6 ² Instituto de Ciencias de la Tierra, TAQUACH, Universidad Austral de Chile, Valdivia, Chile

7 ³ Millennium Nucleus The Seismic Cycle Along Subduction Zones, Valdivia, Chile

8 *Correspondence to:* Roland Freisleben (freisleb@uni-potsdam.de)

9 **Abstract.** Tectonically active coasts are dynamic environments characterized by the presence of multiple marine
10 terraces formed by the combined effects of wave-erosion, tectonic uplift, and sea-level oscillations at glacial-cycle
11 timescales. Well-preserved erosional terraces from the last interglacial sea-level highstand are ideal marker horizons
12 for reconstructing past sea-level positions and calculating vertical displacement rates. We carried out an almost
13 continuous mapping of the last interglacial marine terrace along ~5,000 km of the western coast of South America
14 between 1°N and 40°S. We used quantitatively replicable approaches constrained by published terrace-age estimates
15 to ultimately compare elevations and patterns of uplifted terraces with tectonic and climatic parameters in order to
16 evaluate the controlling mechanisms for the formation and preservation of marine terraces, and crustal deformation.
17 Uncertainties were estimated on the basis of measurement errors and the distance from referencing points. Overall,
18 our results indicate a median elevation of 30.1 m, which would imply a median uplift rate of 0.22 m/ka averaged over
19 the past ~125 ka. The patterns of terrace elevation and uplift rate display high-amplitude (~100–200 m) and long-
20 wavelength (~10² km) structures at the Manta Peninsula (Ecuador), the San Juan de Marcona area (central Peru), and
21 the Arauco Peninsula (south-central Chile). Medium-wavelength structures occur at the Mejillones Peninsula and
22 Topocalma in Chile, while short-wavelength (< 10 km) features are for instance located near Los Vilos, Valparaíso,
23 and Carranza, Chile. We interpret the long-wavelength deformation to be controlled by deep-seated processes at the
24 plate interface such as the subduction of major bathymetric anomalies like the Nazca and Carnegie ridges. In contrast,
25 short-wavelength deformation may be primarily controlled by sources in the upper plate such as crustal faulting,
26 which, however, may also be associated with the subduction of topographically less pronounced bathymetric
27 anomalies. Latitudinal differences in climate additionally control the formation and preservation of marine terraces.
28 Based on our synopsis we propose that increasing wave height and tidal range result in enhanced erosion and
29 morphologically well-defined marine terraces in south-central Chile. Our study emphasizes the importance of using
30 systematic measurements and uniform, quantitative methodologies to characterize and correctly interpret marine
31 terraces at regional scales, especially if they are used to unravel tectonic and climatic forcing mechanisms of their
32 formation. This database is an integral part of the World Atlas of Last Interglacial Shorelines (WALIS), published
33 online at <http://doi.org/10.5281/zenodo.4309748> (Freisleben et al., 2020).

34 1. Introduction

35 Tectonically active coasts are highly dynamic geomorphic environments and they host densely-populated centers and
36 associated infrastructure (Melet et al., 2020). Coastal areas have been episodically affected by the effects of sea-level
37 changes at glacial timescales, ~~drastically~~ modifying the landscape and leaving behind fossil geomorphic markers, such
38 as former paleo-shorelines, ~~abrasion platforms~~, and marine terraces (Lajoie, 1986). One of the most prominent coastal
39 landforms are marine terraces that were generated during the protracted last interglacial sea-level highstand ~~that~~
40 occurred ~125 ka ago (Siddall et al., 2006; Hearty et al., 2007; Pedoja et al., 2011). These terraces are characterized
41 by a higher preservation potential, which facilitates their recognition, mapping, and lateral correlation. Furthermore,
42 because of their high degree of preservation and relatively young age, they have been used to estimate vertical
43 deformation rates at local and regional scales. The relative abundance and geomorphic characteristics of the last
44 interglacial marine terraces make them ideal geomorphic markers with which to reconstruct past sea-level positions
45 and to enable comparisons between distant sites under different climatic and tectonic settings.

46 The Western South American Coast (WSAC) is a tectonically active region that has been repeatedly affected by
47 megathrust earthquakes and associated surface deformation (Beck et al., 1998; Melnick et al., 2006; Bilek, 2010;
48 Baker et al., 2013). Interestingly, previous studies have shown that despite the broad spectrum of latitudinal climatic
49 conditions and erosional regimes along the WSAC, marine terraces are scattered, but omnipresent along the coast (Ota
50 et al., 1995; Regard et al., 2010; Rehak et al., 2010; Bernhardt et al., 2016; Melnick, 2016; Bernhardt et al., 2017).
51 However, only a few studies on interglacial marine terraces have been conducted along the WSAC, primarily in
52 specific areas where they are best expressed; this has resulted in disparate and inconclusive marine terrace
53 measurements based on different methodological approaches and ambiguous interpretations concerning their origin
54 in a tectonic and climatic context (Hsu et al., 1989; Ortlieb and Macharé, 1990; Hsu, 1992; Macharé and Ortlieb, 1992;
55 Pedoja et al., 2006b; Saillard et al., 2009; Pedoja et al., 2011; Saillard et al., 2011; Rodríguez et al., 2013). This lack
56 of reliable data points has revealed a need to re-examine the last interglacial marine terraces along the WSAC based
57 on standardized methodologies in order to obtain a systematic and continuous record of marine terrace elevations
58 along the coast. This information is crucial in order to increase our knowledge of the climatic and tectonic forcing
59 mechanisms that contributed to the formation and degradation of marine terraces in this region.

60 Marine terrace sequences at tectonically active coasts are landforms formed by wave erosion and/or accumulation of
61 sediments resulting from the interaction between tectonic uplift and superposed oscillating sea-level changes (Lajoie,
62 1986; Anderson et al., 1999; Jara-Muñoz et al., 2015). Typically, marine terrace elevations are estimated based on the
63 shoreline angle. The marine terrace morphology comprises a gently inclined ~~marine abrasion-erosional or depositional~~
64 ~~paleo-platform or depositional surface~~ that terminates landward at a steeply sloping paleo-cliff surface. The
65 intersection point between both surfaces represents the ~~approximate~~ sea-level position during the formation of the
66 marine terrace also known as shoreline angle; if coastal uplift is rapid, such uplifting abrasion or depositional surfaces
67 may be preserved in the landscape and remain unaltered by the effects of subsequent sea-level oscillations (Lajoie,
68 1986).

69 The analysis of elevation patterns based on shoreline-angle measurements at subduction margins has been largely used
70 to estimate vertical deformation rates and the mechanisms controlling deformation, including the interaction of the
71 upper plate with bathymetric anomalies, the activity of crustal faults in the upper plate, and deep-seated processes
72 such as basal accretion of subducted trench sediments (Taylor et al., 1987; Hsu, 1992; Macharé and Ortlieb, 1992; Ota
73 et al., 1995; Pedoja et al., 2011; Saillard et al., 2011; Jara-Muñoz et al., 2015; Melnick, 2016). The shoreline angle
74 represents a 1D descriptor of the marine terrace elevation, whose measurements are reproducible when using
75 quantitative morphometric approaches (Jara-Muñoz et al., 2016). Furthermore, the estimation of the marine terrace
76 elevations based on shoreline angles can be further improved by quantifying their relationship with paleo-sea level,
77 also known as the indicative meaning (Lorscheid and Rovere, 2019).

78 In this continental-scale compilation of marine terrace elevations along the WSAC, we present systematically mapped
79 shoreline angles of marine terraces of the last (Eem/Sangamon) interglacial obtained along 5,000 km of coastline
80 between 1°N and 40°S. In this synthesis we rely on chronological constraints from previous regional studies and
81 compilations (Pedoja et al., 2011). For the first time we are able to introduce an almost continuous pattern of terrace
82 elevation and coastal uplift rates at a spatial scale of 10³ km along the WSAC. Furthermore, in our database we
83 compare tectonic and climatic parameters to elucidate the mechanisms controlling the formation and preservation of
84 marine terraces, and patterns of crustal deformation along the coast. This study was thus primarily intended to provide
85 a comprehensive, standardized database and description of last interglacial marine terrace elevations along the
86 tectonically active coast of South America. This database therefore affords future research into coastal environments
87 to decipher potential tectonic forcings with regard to the deformation and seismotectonic segmentation of the forearc;
88 as such this database will ultimately help to decipher the relationship between upper-plate deformation, vertical motion
89 and bathymetric anomalies and aid in the identification of regional fault motions along pre-existing anisotropies in the
90 South American continental plate. Finally, our database includes information on climate-driving forcing mechanisms
91 that may influence the formation, modification and/or destruction of marine terraces in different climatic sectors along
92 the South American convergent margin. This new database is part of the World Atlas of Last Interglacial Shorelines
93 (WALIS), published online at <http://doi.org/10.5281/zenodo.4309748> (Freisleben et al., 2020).

94 **2. Geologic and geomorphic setting of the WSAC**

95 **2.1. Tectonic and seismotectonic setting**

96 **2.1.1. Subduction geometry and bathymetric features**

97 The tectonic setting of the convergent margin of South America is controlled by subduction of the oceanic Nazca plate
98 beneath the South American continental plate. The convergence rate varies between 66 mm/a in the north (8°S latitude)
99 and 74 mm/a in the south (27°S latitude) (Fig. 1). The convergence azimuth changes slightly from N81.7° toward
100 N77.5° from north to south (DeMets et al., 2010). The South American subduction zone is divided into four major
101 segments [with variable subduction angles](#) inferred from the spatial distribution of Benioff seismicity (Barazangi and
102 Isacks, 1976; Jordan et al., 1983) (Fig. 1). The segments beneath northern and central Peru (2°–15°S) and beneath

103 central Chile (27°–33°S) are characterized by a gentle dip of the subducting plate between 5° and 10° at depths of
104 ~100 km (Hayes et al., 2018), whereas the segments beneath southern Peru and northern Chile (15°–27°S), and beneath
105 southern Chile (33°–45°S) have steeper dips of 25° to 30°. Spatial distributions of earthquakes furthermore indicate a
106 steep-slab subduction segment in Ecuador and southern Colombia (2°S to 5°N), and a flat-slab segment in NW
107 Colombia (north of 5°N) (Pilger, 1981; Cahill and Isacks, 1992; Gutscher et al., 2000; Ramos and Folguera, 2009).
108 Processes that have been inferred to be responsible for the shallowing of the subduction slab include the subduction
109 of large buoyant ridges or plateaus (Espurt et al., 2008) as well as the combination of trenchward motion of thick,
110 buoyant ~~eratonic-continental~~ lithosphere accompanied by trench retreat (Sobolev and Babeyko, 2005; Manea et al.,
111 2012). Volcanic activity as well as the forearc architecture and distribution of upper-plate deformation further
112 emphasize the location of flat-slab subduction segments (Jordan et al., 1983; Kay et al., 1987; Ramos and Folguera,
113 2009).

114 Several ~~high~~ bathymetric ~~anomalies-features~~ have been recognized on the subducting Nazca plate. The two most
115 prominent ~~anomalies-bathymetric features~~ being subducted beneath South America are the Carnegie and Nazca
116 aseismic ridges at 0° and 15°S, respectively; ~~they consist of seamounts related to hot-spot volcanism~~ (Gutscher et al.,
117 1999; Hampel, 2002). The ~~300-km-wide and ~2-km-high~~ Carnegie Ridge subducts roughly parallel with the
118 convergence direction and its ~~position-geometry~~ should have remained relatively stable beneath the continental ~~plate~~
119 (Angermann et al., 1999; Gutscher et al., 1999; DeMets et al., 2010; Martinod et al., 2016a). In contrast, the obliquity
120 of the ~~200-km-wide and 1.5-km-high~~ Nazca Ridge with respect to the convergence direction resulted in 500 km SE-
121 directed migration of ~~the-its locus of ridge~~ subduction ~~locus~~ during the last 10 Ma (Hampel, 2002; Saillard et al., 2011;
122 Martinod et al., 2016a). Similarly, smaller aseismic ridges such as the Juan Fernández Ridge and the Iquique Ridge
123 subduct beneath the South American continent at 32°S and 21°S, respectively. The ~~subduction-of-intercepts between~~
124 these bathymetric anomalies ~~and the upper plate~~ are thought to influence the characteristics of interplate coupling and
125 seismic rupture (Bilek et al., 2003; Wang and Bilek, 2011; Geersen et al., 2015; Collot et al., 2017) and mark the
126 boundaries between flat and steep subduction segments and changes between subduction erosion and accretion (Jordan
127 et al., 1983; von Huene et al., 1997; Ramos and Folguera, 2009) (Fig. 1).

128 In addition to bathymetric anomalies, several studies have shown that variations in the ~~amount-volume~~ of sediments
129 in the trench may control the subduction regime from an erosional mode to an accretionary mode (von Huene and
130 Scholl, 1991; Bangs and Cande, 1997). In addition, the ~~amount-volume~~ of sediment in the trench has also been
131 hypothesized to influence the style of interplate seismicity (Lamb and Davis, 2003). At the southern Chile margin,
132 thick trench ~~sediments~~ ~~sequences~~ and a steeper subduction angle correlate primarily with subduction accretion,
133 although the area of the intercept of the continental plate with the Chile Rise spreading center locally exhibits the
134 opposite case (von Huene and Scholl, 1991; Bangs and Cande, 1997). Subduction erosion characterizes the region
135 north of the southern volcanic zone from central and northern Chile to southern Peru (33°–15°S) due to decreasing
136 sediment supply to the trench, especially within the flat-slab subduction segments (Stern, 1991; von Huene and Scholl,
137 1991; Bangs and Cande, 1997; Clift and Vannucchi, 2004). Clift and Hartley (2007) and Lohrmann et al. (2003)
138 argued for an alternate style of slow tectonic erosion leading to underplating of subducted material below the base of

139 the crustal forearc, synchronous with tectonic erosion beneath the trenchward part of the forearc. For the northern
140 Andes, several authors also classify the subduction zone as an erosional type (Clift and Vannucchi, 2004; Scholl and
141 Huene, 2007; Marcaillou et al., 2016).

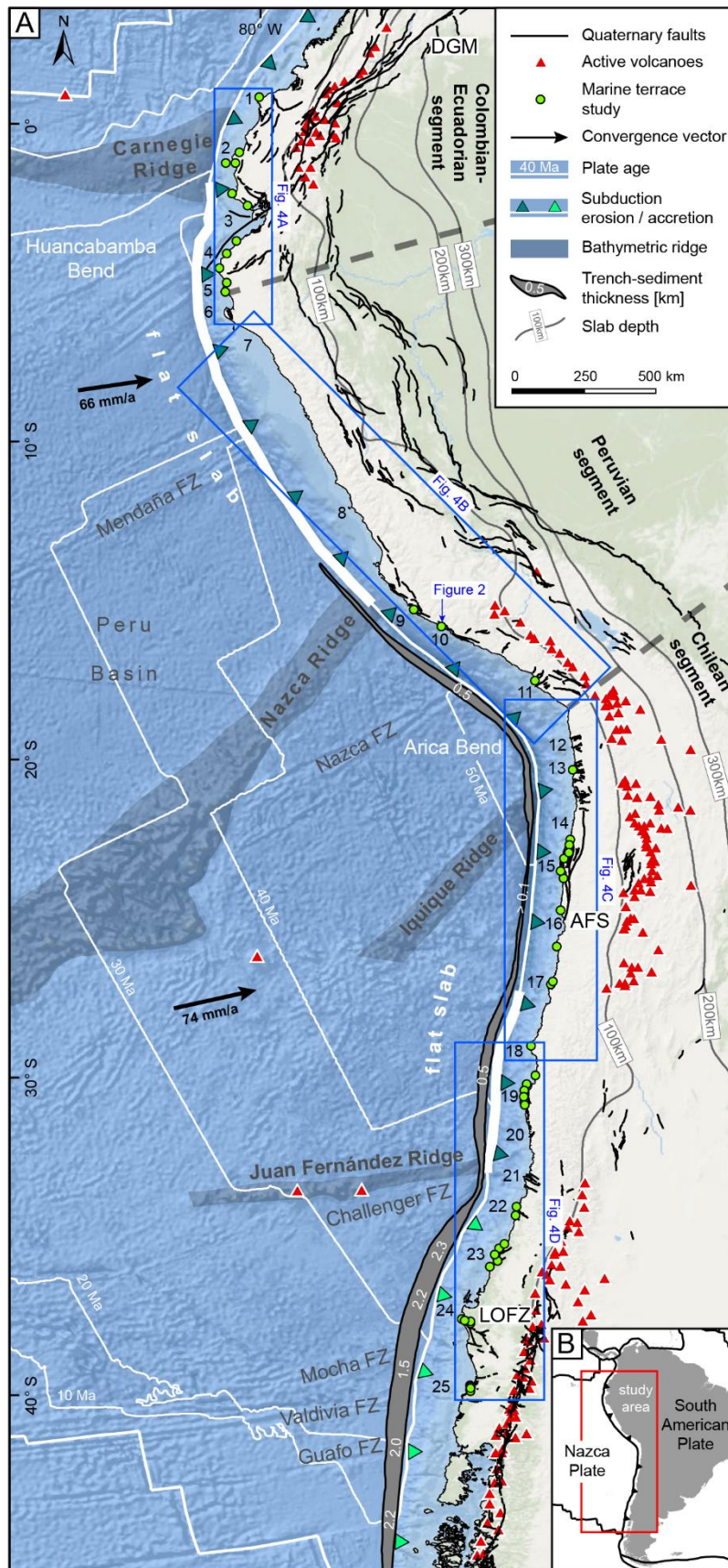
142 **2.1.2. Major continental fault systems in the coastal realm**

143 The South American convergent margin comprises several fault systems with different kinematics, [whose presence is](#)
144 [closely linked to oblique subduction and the motion and deformation of forearc slivers](#). Here we summarize the main
145 structures that affect the Pacific coastal areas. North of the Talara bend (5°S), active thrusting and dextral strike-slip
146 faulting dominates [the coastal lowlands of Ecuador \(e.g., Mache, Bahía, Jipijapa faults\)](#), [although normal faulting also](#)
147 [occurs at Punta Galera \(Cumilínche fault\) and the Manta Peninsula \(Río Salado fault\) \(Fig. 1\)](#). [Farther south, normal](#)
148 [faulting is active in the Gulf of Guayaquil \(Posorja fault\) and dextral strike-slip faulting occurs at the Santa Elena](#)
149 [Peninsula \(La Cruz fault\)](#) (Veloza et al., 2012; Costa et al., 2020). The most prominent dextral fault in this region is
150 the 2000-km-long, northeast-striking Dolores-Guayaquil megashear (DGM), which starts in the Gulf of Guayaquil
151 and terminates in the Colombian hinterland east of the range-bounding thrust faults of the Colombian Andes (Veloza
152 et al., 2012; Villegas-Lanza et al., 2016; Costa et al., 2020) (Fig. 1). Normal faults have been described along the coast
153 of Peru at the Illescas Peninsula in the north (6°S), in the San Juan de Marcona area with the El Huevo–Lomas fault
154 system (14.5°–16°S), and the Incapuquio fault system in the south (17°–18°S) (Veloza et al., 2012; Villegas-Lanza et
155 al., 2016; Costa et al., 2020). The main fault zones of the Chilean convergent margin comprise the Atacama Fault
156 System (AFS) in the Coastal Cordillera extending from Iquique to La Serena (29.75°S, [Fig. 1](#)), with predominantly
157 N-S-striking normal faults, which result in relative uplift of their western side (e.g., Mejillones fault, Salar del Carmen
158 fault) (Naranjo, 1987; González and Carrizo, 2003; Cembrano et al., 2007). ~~Smaller e~~Coastal fault systems farther
159 south are located in the Altos de Talinay area (30.5°S, Puerto Aldea fault), near Valparaíso (33°S, Quintay and
160 Valparaíso faults), near the Arauco Peninsula (36°–39°S, Santa María and Lanalhue faults), and in between [these areas](#)
161 (Topocalma, Pichilemu, Carranza, and Pelluhue faults) (Ota et al., 1995; Melnick et al., 2009; Santibáñez et al., 2019;
162 Melnick et al., 2020; Maldonado et al., 2021) ([Fig. 1](#)). However, there is still limited knowledge regarding Quaternary
163 slip rates and kinematics and, most importantly, the location of active faults along the forearc region of South America
164 (Jara-Muñoz et al., 2018; Melnick et al., 2019).

165 **2.2. Climate and geomorphic setting**

166 **2.2.1. Geomorphology**

167 The 8000-km-long Andean orogen is a major, hemisphere-scale feature that can be divided into different segments
168 with distinctive geomorphic and tectonic characteristics. The principal segments comprise the NNE-SSW trending
169 Colombian-Ecuadorian segment (12°N–5°S), the NW-SE oriented Peruvian segment (5°–18°S), and the N-S trending
170 Chilean segment (18°–56°S) (Jaillard et al., 2000) (Fig. 1). Two major breaks separate these segments; these are the
171 Huancabamba bend in northern Peru and the Arica bend at the Peru-Chile border. The distance of the trench from the
172 [WSA](#) coastline averages 118 km and ranges between 44 and 217 km. The depth of the trench fluctuates between



174 2920 and 8177 m (GEBCO Bathymetric Compilation Group, 2020), and the continental shelf has an average width of
175 28 km (Paris et al., 2016).

176 In the 50- to 180-km-wide coastal area of the Ecuadorian Andes, where the Western Cordillera is flanked by a
177 structural depression, relief is relatively low (< 300 m asl). The Gulf of Guayaquil (3°S) and the Dolores-Guayaquil
178 megashear separate the northern from the southern forearc units. The coast-trench distance along the Huancabamba
179 bend is quite small (~55–90 km), except for the Gulf of Guayaquil, and the trench east of the Carnegie Ridge is at a
180 relatively shallow depth of ~3.5 km. Farther south, the Peruvian forearc comprises the up to 160-km-wide Coastal
181 Plains in the north and the narrow, 3000-m-high Western Cordillera. While the Coastal Plains in north-central Peru
182 are relatively narrow (< 40 km), they widen in southern Peru, and the [elevation of the](#) Western Cordillera increases to
183 more than 5000 m (Suárez et al., 1983; Jaillard et al., 2000). The region between the coast and the trench in central
184 Peru (up to 220 km) narrows toward the San Juan de Marcona area (~75 km) near the [intercept with the](#) Nazca Ridge,
185 and the relatively deep trench (~6.5 km) becomes shallower (< 5 km) (GEBCO Bathymetric Compilation Group,
186 2020). Between 18°S and 28°S, the Chilean forearc comprises the 50-km-wide and up to 2700-m-high Coastal
187 Cordillera, which is separated from the Precordillera by the Central Depression. In the flat-slab subduction segment
188 between 27°S and 33°S there is neither a morphotectonic region characterized by a central depression nor active
189 volcanism in the high Andean cordillera (Fig. 1) (Jordan et al., 1983). The Chilean forearc comprises the Coastal
190 Cordillera, which varies in altitude from up to 2000 m at 33°S to 500 m at 46°S, and the Central Depression that
191 separates the forearc from the Main Cordillera. From the Arica bend, where the coast-trench distance is up to 170 km
192 and the trench ~8 km deep, a slight increase in [coast-trench](#) distance can be observed in Chile toward the south (~80–
193 130 km), as can a decrease in trench depth to ~4.5 km.

194 2.2.2. Marine terraces and coastal uplift rates

195 Wave erosion forms wave-cut terrace levels, while the accumulation of shallow marine sediments during sea-level
196 highstands forms wave-built terraces. Another type of terrace is known as “rasa” and refers to wide shore platforms
197 formed under slow-uplift conditions (< 0.2 m/ka), and the repeated reoccupation of this surface by high sea levels
198 (Regard et al., 2010; Rodríguez et al., 2013; Melnick, 2016). [Other studies indicate a stronger influence of climate and](#)
199 [rock resistance to erosion compared to marine wave action](#) (Prémaillon et al., 2018). Typically, the formation of
200 Pleistocene marine terraces in the study area occurred during interglacial and interstadial relative sea-level highstands
201 that were superposed on the uplifting coastal areas; according to the Quaternary oxygen-isotope curve defining warm
202 and cold periods, high Quaternary sea levels have been correlated with warm periods and are denoted with the odd-
203 numbered Marine Isotope Stages (MIS) (Lajoie, 1986; Shackleton et al., 2003).

204 Along the WSAC, staircase-like sequences of multiple marine terraces are preserved nearly continuously along the
205 coast. [They-These terraces](#) comprise primarily wave-cut surfaces that are frequently covered by beach ridges of
206 siliciclastic sediments and local accumulations of carbonate bioclastic materials [along-the-associated with](#) beach ridges
207 (Ota et al., 1995; Saillard et al., 2009; Rodríguez et al., 2013; Martinod et al., 2016b). Rasa surfaces exist in the regions
208 of southern Peru and northern Chile (Regard et al., 2010; Rodríguez et al., 2013; Melnick, 2016). Particularly the well-

209 preserved MIS-5e terrace level has been largely used as a strain marker in the correlation of uplifted coastal sectors
210 due to its lateral continuity and high potential for preservation. Global observations of sea-level fluctuations during
211 MIS-5 ~~allow to~~ differentiate between three second-order highstands at 80 ka (5a), 105 ka (5c), and 128 to 116 ka (5e)
212 with paleo-sea levels of -20 m for both of the younger and +3 ± 3 m for the oldest highstand (Stirling et al., 1998;
213 Siddall et al., 2006; Hearty et al., 2007; Rohling et al., 2009; Pedoja et al., 2011). The database generated in this study
214 is based exclusively in the last interglacial marine terraces exposed along the WSA~~C~~, between Ecuador and Southern
215 Chile (1°S to 40°S). In the following section we present a brief review of previously studied marine terrace sites in
216 this area.

217 Paleo-shoreline elevations of the last interglacial (MIS-5e) in Ecuador are found at elevations of around 45 ± 2 m asl
218 in Punta Galera (Esmeraldas area), 43–57 ± 2 m on the Manta Peninsula and La Plata Island, and 15 ± 5 m asl on the
219 Santa Elena Peninsula (Pedoja et al., 2006a; Pedoja et al., 2006b). In northern Peru, MIS-5e terraces have been
220 described at elevations of 18–31 m asl for the Tablazo Lobitos (Cancas and Mancora areas), at 25 ± 5 m asl on the
221 Paita Peninsula, and at 18 ± 3 m asl on the Illescas Peninsula and the Bay of Bayovar (Pedoja et al., 2006b). Farther
222 south, MIS-5e terraces are exceptionally high in the San Juan de Marcona area immediately south of the subducting
223 Nazca Ridge, with maximum elevations of 80 m at the Cerro Tres Hermanas and 105 m at the Cerro El Huevo (Hsu
224 et al., 1989; Ortlieb and Macharé, 1990; Saillard et al., 2011). The Pampa del Palo region in southern Peru ~~shows~~
225 ~~exhibits~~ relatively thick vertical stacks of shallow marine terrace deposits related to MIS-7, 5e (~20 m), and 5c that
226 may indicate a different geodynamic behavior compared to adjacent regions (Ortlieb et al., 1996b). In central and
227 northern Chile, the terrace levels of the last interglacial ~~exist-occur~~ at 250–400 m, 150–240 m, 80–130 m, and 30–40
228 m, and in southern Chile at 170–200 m, 70 m, 20–38 m, 8–10 m (Fuenzalida et al., 1965). Specifically, between 24°S
229 and 32°S, paleo-shoreline elevations of the last interglacial (MIS-5e) range between 25 and 45 m (Ota et al., 1995;
230 Saillard et al., 2009; Martinod et al., 2016b). Shore platforms are higher in the Altos de Talinay area (30.3°–31.3°S),
231 but are small, poorly preserved, and terminate at a high coastal scarp between 26.75°S and 24°S (Martinod et al.,
232 2016b). Shoreline-angle elevations ~~within the-between 34° and 38°S (along the Maule seismotectonic segment) (34°–~~
233 ~~38°S)~~ vary from high altitudes in the Arauco and Topocalma areas (200 m) to moderate elevations near Caranza (110
234 m), and very low elevations in between (15 m) (Melnick et al., 2009; Jara-Muñoz et al., 2015).

235 Coastal uplift-rate estimates along the WSA~~C~~ mainly comprise calculations for the Talara Arc, the San Juan de
236 Marcona area, the Mejillones Peninsula, the Altos de Talinay area, and several regions in south-central Chile. Along
237 the Talara Arc (6.5°S to 1°N), marine terraces of the Manta Peninsula and La Plata Island in central Ecuador indicate
238 the most ~~extensive-pronounced~~ uplift rates of 0.31 to 0.42 m/ka ~~since MIS-5e~~, while ~~lower-similar~~ uplift rates are
239 documented to the north in the Esmeraldas area (0.34 m/ka), and ~~especially-lower ones~~ to the south at the Santa Elena
240 Peninsula (0.1 m/ka). In northern Peru, ~~last interglacial~~ uplift rates are relative low, ranging from 0.17–0.21 m/ka for
241 the Tablazo Lobitos and 0.16 m/ka for the Paita Peninsula, to 0.12 m/ka for the Bay of Bayovar and the Illescas
242 Peninsula (Pedoja et al., 2006a; Pedoja et al., 2006b). Marine terraces ~~on the continental plate~~ above the subducting
243 Nazca Ridge (13.5°–15.6°S) ~~show-record~~ variations in uplift rate where the coastal forearc above the northern flank
244 of the ridge is ~~either~~ stable or has undergone net subsidence (Macharé and Ortlieb, 1992), ~~or where the~~ The coast

245 above the ridge crest is rising at about 0.3 m/ka and the coast above the southern flank (San Juan de Marcona) is
246 uplifting at a rate of 0.5 m/ka (Hsu, 1992) or ~~at~~ even 0.7 m/ka (Ortlieb and Macharé, 1990) for at least the last 125 ka
247 ~~according to Ortlieb and Macharé (1990)~~. Saillard et al. (2011) state that long-term regional uplift in the San Juan de
248 Marcona area has increased since about 800 ka related to the southward migration of the Nazca Ridge, and ranges
249 from 0.44 to 0.87 m/ka. The Pampa del Palo area in southern Peru rose more slowly or was even down-faulted and
250 had subsided with respect to the adjacent coastal regions (Ortlieb et al., 1996b). These movements ceased after the
251 highstand during the MIS-5e and slow uplift rates of ~~around approximately~~ 0.16 m/ka have characterized the region
252 since 100 ka (Ortlieb et al., 1996b). In northern Chile (24°–32°S), uplift rates for the Late Pleistocene average around
253 0.28 ± 0.15 m/ka (Martinod et al., 2016b), except for the Altos de Talinay area, where pulses of rapid uplift occurred
254 during the Middle Pleistocene (Ota et al., 1995; Saillard et al., 2009; Martinod et al., 2016b). The Central Andean rasa
255 (15°–33°S) and ~~oldest~~ Lower to Middle Pleistocene shore platforms – which are also generally wider – indicate a
256 period of tectonic stability or subsidence followed by accelerated and spatially continuous uplift after a period of
257 tectonic stability or subsidence after ~400 ka (MIS-11) (Regard et al., 2010; Rodríguez et al., 2013; Martinod et al.,
258 2016b). However, a According to Melnick (2016), the Central Andean rasa has experienced slow and steady long-term
259 uplift at with a rate of 0.13 ± 0.04 m/ka during the Quaternary, predominantly accumulating strain through deep
260 earthquakes at the crust-mantle boundary (Moho) below the locked portion of the plate interface. The lowest uplift
261 rates occur at the Arica bend and increase gradually southward; the highest values are attained along geomorphically
262 distinct peninsulas (Melnick, 2016). In the Maule segment (34°–38°S), the mean uplift rate for the MIS-5 terrace level
263 is 0.5 m/ka, exceeded only in the areas of Topocalma, Carranza, and Arauco, where it amounts to (reaching up to 1.6
264 m/ka) (Melnick et al., 2009; Jara-Muñoz et al., 2015). Although there are several studies of marine terraces along the
265 WSAC, these are isolated and based on different methodological approaches, mapping and leveling resolution, as well
266 as dating techniques, which makes regional comparisons and correlations difficult in the context of the data presented
267 here.

268 2.2.3. Climate

269 Apart from latitudinal temperature changes, the present-day morphotectonic provinces along the South American
270 margin have a pronounced impact on the precipitation gradients on the west coast of South America. Since mountain
271 ranges are oriented approximately perpendicular to moisture-bearing winds, they affect both flanks of the orogen
272 (Strecker et al., 2007). The regional-scale pattern of wind circulation is dominated by westerly winds at
273 subtropical/extratropical latitudes primarily up to about 27°S (Garreaud, 2009). However, anticyclones over the South
274 Pacific result in winds blowing from the south along the coast between 35°S and 10°S (Garreaud, 2009). The moisture
275 in the equatorial Andes (Ecuador and Colombia) and in the areas farther south (27°S) is fed by winds from the Amazon
276 basin and the Gulf of Panama, resulting in rainfall mainly on the eastern flanks of the mountain range (Bendix et al.,
277 2006; Bookhagen and Strecker, 2008; Garreaud, 2009). The Andes of southern Ecuador, Peru, and northern Chile are
278 dominated by a rain-shadow effect that causes aridity within the Andean Plateau (Altiplano-Puna), the Western
279 Cordillera, and the coastal region (Houston and Hartley, 2003; Strecker et al., 2007; Garreaud, 2009). Furthermore,
280 the aridity is exacerbated by the effects of the cold Humboldt current, which prevents humidity from the Pacific from

281 penetrating inland (Houston and Hartley, 2003; Garreaud, 2009; Coudurier-Curveur et al., 2015). The precipitation
282 gradient reverses between 27°S and 35°S, where the Southern Hemisphere Westerlies cause abundant rainfall on the
283 western flanks of the Coastal and Main cordilleras (Garreaud, 2009). Martinod et al. (2016b) ~~has~~ proposed that
284 latitudinal differences in climate largely influence coastal morphology, specifically the formation of high coastal
285 scarps that prevent the development of extensive marine terrace sequences. However, the details of this relationship
286 have not been conclusively studied along the full extent of the Pacific coast of South America.

287 3. Methods

288 We combined – and describe in detail below – bibliographic information, different topographic data sets, and uniform
289 morphometric and statistical approaches to assess the elevation of marine terraces and accompanying vertical
290 deformation rates along the [western](#) South American margin.

291 3.1. Mapping marine terraces

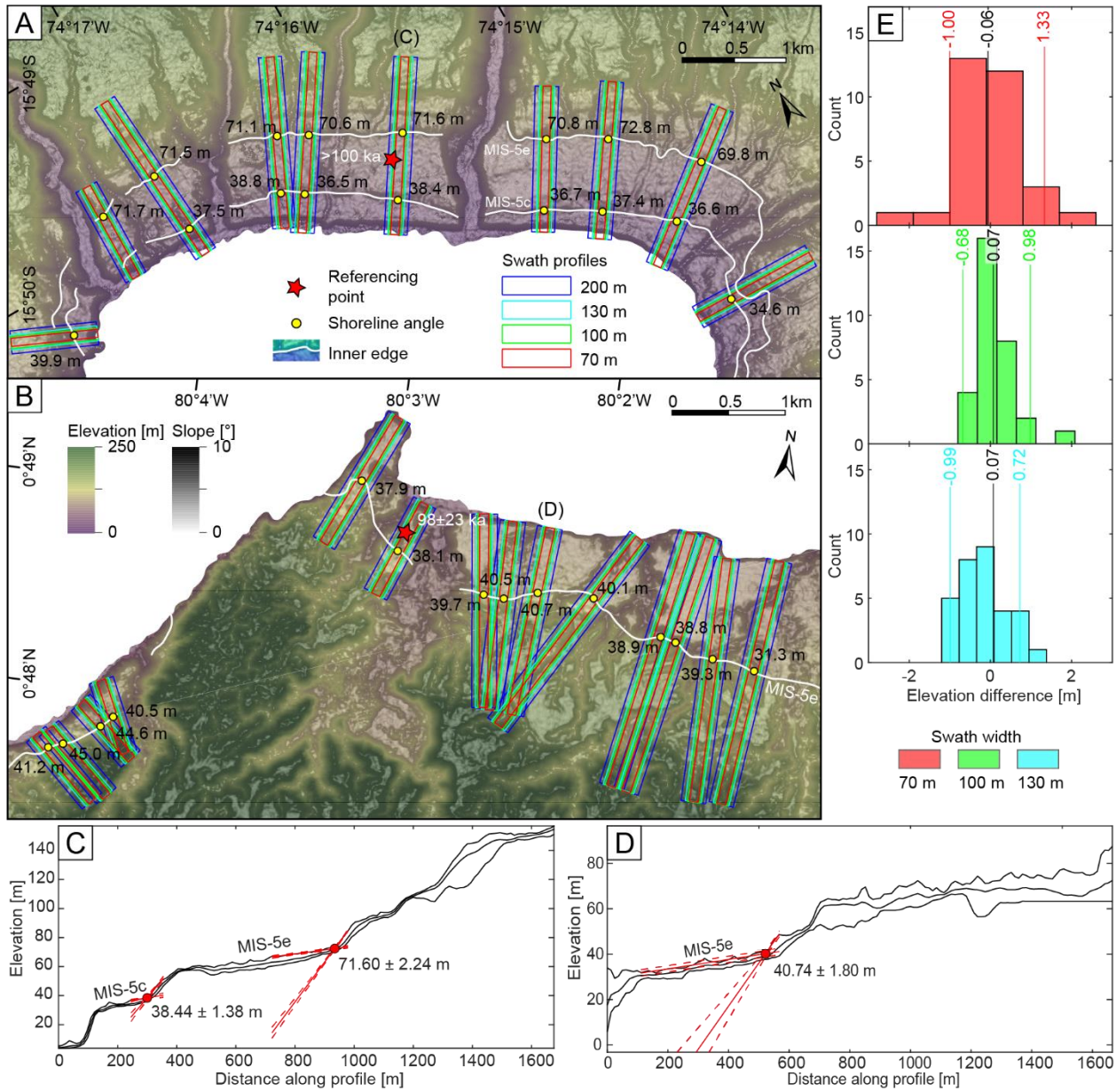
292 Marine terraces are primarily described based on their elevation, which is essential for determining vertical
293 deformation rates. The measurements of the marine terrace elevations of the last interglacial were performed using
294 TanDEM-X topography (12 and 30 m horizontal resolution) (German Aerospace Center (DLR), 2018), and digital
295 terrain models from LiDAR (1, 2.5, and 5 m horizontal resolution). The DEMs were converted to orthometric heights
296 ~~by subtracting the EGM2008 geoid and projected in UTM using the ellipsoid projection of the~~ World Geodetic System
297 ~~(WGS1984) and the EGM2008 (E_{EGM08}) geoid. The orthometrically corrected DEMs were projected in Universal~~
298 ~~Transverse Mercator (UTM) projections of varying zones, namely WGS84 UTM Z_{using} zone 19S for Chile, Z_{one}~~
299 ~~zone 18S for southern/central Peru, and $Z_{one-zone}$ 17S for northern Peru/Ecuador.~~

300 To trace the MIS-5 shoreline, we mapped its inner edge along the west coast of South America based ~~on the TanDEM-~~
301 ~~X topography on slope changes on TanDEM-X topography at the foot of paleo-cliffs~~ (Jara-Muñoz et al., 2016) (Fig.
302 2A and B). To facilitate mapping, we used slope and hillshade maps. We correlated the ~~results of the inner-inner~~ edge
303 mapping with the marine terraces catalog of Pedoja et al. (2011) and ~~the~~ references therein (section 2.2.2, Table 1).
304 Further references used to validate MIS-5e terrace heights include Victor et al. (2011) for the Pampa de Mejillones,
305 Martinod et al. (2016b) for northern Chile, and Jara-Muñoz et al. (2015) for the area between 34° and 38°S. We define
306 the term “referencing point” for these previously published terrace heights and age constraints. The referencing point
307 with the ~~nearest-shortest~~ distance to the location of our measurements served as ~~an orientation for a topographical and~~
308 ~~chronological benchmark for mapping~~ the MIS-5 terrace ~~elevation~~ in the respective areas. In addition, this distance is
309 used to assign a quality rating to our measurements.

310 In addition to MIS-5e, we also mapped MIS-5c in areas with high uplift rates such as at the Manta Peninsula, San
311 Juan de Marcona, Topocalma, Carranza, and Arauco. Although we observed a terrace level correlated to MIS-5a in
312 the Marcona area, we excluded this level from the database due to its limited preservation at other locations and lack
313 of chronological constraints. Our assignment of mapped terrace levels to MIS-5c is primarily based on age constraints
314 by Saillard et al. (2011) for the Marcona area and Jara-Muñoz et al. (2015) for the area between 34° and 38°S.

315 [However, in order to evaluate the possibility that our correlation with MIS-5c is flawed, we estimated uplift rates for](#)
316 [the lower terraces by assigning them tentatively to either MIS-5a or MIS-5c. We interpolated the uplift rates derived](#)
317 [from the MIS-5e level at the sites of the lower terraces and compared the differences \(Figure 3A\). If we infer that](#)
318 [uplift rates were constant in time at each site throughout the three MIS-5 substages, the comparison suggests these](#)
319 [lower terrace levels correspond to MIS-5c because of the smaller difference in uplift rate, rather than to MIS-5a \(Figure](#)
320 [3B\).](#)

321 A rigorous assessment of marine terrace elevations is crucial for determining accurate vertical deformation rates. Since
322 fluvial degradation and hillslope processes after the abandonment of marine terraces may alter their morphology
323 (Anderson et al., 1999; Jara-Muñoz et al., 2015), direct measurements of terrace elevations at the inner edge (foot of
324 the paleo-cliff) may result in overestimation of the terrace elevations and vertical deformation rates (Jara-Muñoz et
325 al., 2015). To precisely measure the shoreline-angle elevations of the MIS-5 terrace level, we used a profile-based
326 approach in TerraceM, a graphical user interface in MATLAB® (Jara-Muñoz et al., 2016), available at
327 www.terrace.m.com. We placed swath profiles of variable width perpendicular to the previously mapped inner edge,
328 which were used by the TerraceM algorithm to extract maximum elevations to avoid fluvial incision (Fig. 2A [and B](#)).
329 [For the placement of the swath profiles we tried to capture a local representation of marine terrace topography with a](#)
330 [sufficiently long, planar paleo-platform, and a sufficiently high paleo-cliff, simultaneously avoiding topographic](#)
331 [disturbance, such as colluvial wedges or areas characterized by river incision.](#) North of Caleta Chañaral (29°S), we
332 used swath profiles of 200 m width, although we occasionally used 100-m-wide profiles for narrow terrace remnants.
333 South of 29°S, we used swath widths of 130 and 70 m. The width was chosen based on fluvial drainage densities that
334 are associated with climate gradients. Sensitivity tests comparing shoreline-angle measurements from different swath
335 widths in the Chala Bay [and at Punta Galera](#) show only minimal [vertical](#) deviations of less than 0.5 m (Fig. [2C2E](#)).
336 The sections of these profiles, which represent the undisturbed paleo-platform and paleo-cliff, were picked manually
337 and fitted by linear regression. The extrapolated intersection between both regression lines ultimately determines the
338 buried shoreline-angle elevation and associated uncertainty, which is derived from the 95% confidence interval (2σ)
339 of both regressions (Fig. [2B2C and D](#)). In total, we measured 1843 ~~and 110 MIS-5e and 110 MIS-5c~~ shoreline-angle
340 elevations ~~of the MIS-5e and MIS-5c terrace levels, respectively~~. To quantify the paleo-position of the relative sea-
341 level elevation and the involved uncertainty for the WALIS template, we calculated the indicative meaning using the
342 IMCalc software from Lorscheid and Rovere (2019). [The indicative meaning comprises the range between the lower](#)
343 [and upper limits of sea-level formation – the indicative range – as well as its mathematically averaged position, which](#)
344 [corresponds to the reference water level](#) (Lorscheid and Rovere, 2019).



345

346 **Figure 2. (A)** Orthometrically corrected TanDEM-X and slope map of **(A) Chala Bay in south-central Peru and (B) Punta**
 347 **Galera in northern Ecuador** with mapped **shoreline**-inner **shoreline** edges of the MIS-5e and 5c terrace levels. Colored
 348 rectangles represent swath-profile boxes of various widths that were placed perpendicular to the inner edges for the
 349 subsequent estimation of terrace elevation in TerraceM. The red star indicates **the referencing point with**
 350 **this the respective** area (Pedoja et al., 2006b; Saillard, 2008). **(B-C) and (D)** Estimation of the shoreline-angle elevation
 351 in TerraceM by intersecting linear-regression fits of the paleo-cliff and paleo-platform (**200-m-wide swath profiles**). **(E)**
 352 Histograms of elevation differences measured **in both areas** for various swath widths (70 m, 100 m, and 130 m) with respect
 353 to the 200-m-wide reference swath profile (blue). **Vertical lines indicate median values and standard deviations (2σ).**

354

355

356

357

358
359
360
361
362
363

Table 1. Age constraints used for mapping of the inner edge of MIS-5 and for verifying our terrace-elevation measurements. This compilation is mainly based on the terrace catalog of [Pedoja et al. \(2011\)](#); added references include [Victor et al. \(2011\)](#) for Pampa de Mejillones, [Martinod et al. \(2016b\)](#) for northern Chile, and [Jara-Muñoz et al. \(2015\)](#) for south-central Chile. **Absolute ages refer to MIS-5e marine terraces, unless otherwise specified; inferred ages refer to their associated MIS. IRSL: Infrared Stimulated Luminescence, AAR: Amino-Acid Racemization, CRN: Cosmogenic Radionuclides, ESR: Electron Spin Resonance.**

Country	Location	Lat.	Long.	Dating method	Confidence	Reference	Age [ka]
Ecuador	Galera	0.81	-80.03	IRSL	5	Pedoja et al., 2006b	98±23
Ecuador	Manta	-0.93	-80.66	IRSL, U/Th	5	Pedoja et al., 2006b	76±18, 85±1
Ecuador	La Plata	-1.26	-81.07	U/Th	5	Pedoja et al., 2006b	104±2
Ecuador	Manta	-1.27	-80.78	IRSL	5	Pedoja et al., 2006b	115±23
Ecuador	Santa Elena	-2.21	-80.88	U/Th	5	Pedoja et al., 2006b	136±4, 112±2
Ecuador	Puna	-2.60	-80.40	U/Th	5	Pedoja et al., 2006b	98±3, 95±0
Peru	Cancas	-3.72	-80.75	Morphostratigraphy	5	Pedoja et al., 2006b	~125
Peru	Mancora/Lobitos	-4.10	-81.05	Morphostratigraphy	5	Pedoja et al., 2006b	~125
Peru	Talara	-4.56	-81.28	Morphostratigraphy	5	Pedoja et al., 2006b	~125
Peru	Paita	-5.03	-81.06	Morphostratigraphy	5	Pedoja et al., 2006b	~125
Peru	Bayovar/Illescas	-5.31	-81.10	IRSL	5	Pedoja et al., 2006b	111±6
Peru	Cerro Huevo	-15.31	-75.17	CRN	5	Saillard et al., 2011	228±28 (7e)
Peru	Chala Bay	-15.85	-74.31	CRN	5	Saillard, 2008	>100
Peru	Ilo	-17.55	-71.37	AAR	5	Ortlieb et al., 1996b; Hsu et al., 1989	~125, ~105
Chile	Punta Lobos	-20.35	-70.18	U/Th, ESR	5	Radtke, 1989	~125
Chile	Cobija	-22.55	-70.26	Morphostratigraphy	4	Ortlieb et al., 1995	~125, ~105
Chile	Michilla	-22.71	-70.28	AAR	3	Leonard & Wehmiller, 1991	~125
Chile	Hornitos	-22.85	-70.30	U/Th	5	Ortlieb et al., 1996a	108±1, 118±6
Chile	Chacaya	-22.95	-70.30	AAR	5	Ortlieb et al., 1996a	~125
Chile	Pampa Mejillones	-23.14	-70.45	U/Th	5	Victor et al., 2011	124±3
Chile	Mejillones/Punta Jorge	-23.54	-70.55	U/Th, ESR	3	Radtke, 1989	~125
Chile	Coloso	-23.76	-70.46	ESR	3	Schellmann & Radtke, 1997	106±3
Chile	Punta Piedras	-24.76	-70.55	CRN	5	Martinod et al., 2016b	138±15
Chile	Esmeralda	-25.91	-70.67	CRN	5	Martinod et al., 2016b	79±9
Chile	Caldera	-27.01	-70.81	U/Th, ESR	5	Marquardt et al., 2004	~125
Chile	Bahia Inglesa	-27.10	-70.85	U/Th, ESR	5	Marquardt et al., 2004	~125
Chile	Caleta Chanaral	-29.03	-71.49	CRN	5	Martinod et al., 2016b	138±0
Chile	Coquimbo	-29.96	-71.34	AAR	5	Leonard & Wehmiller, 1992; Hsu et al., 1989	~125
Chile	Punta Lengua de Vaca	-30.24	-71.63	U/Th	5	Saillard et al., 2012	95±2 (5c)
Chile	Punta Lengua de Vaca	-30.30	-71.61	U/Th	5	Saillard et al., 2012	386±124 (11)
Chile	Quebrada Palo Cortado	-30.44	-71.69	CRN	5	Saillard et al., 2009	149±10

Chile	Rio Limari	-30.63	-71.71	CRN	5	Saillard et al., 2009	318±30 (9c)
Chile	Quebrada de la Mula	-30.79	-71.70	CRN	5	Saillard et al., 2009	225±17 (7e)
Chile	Quebrada del Teniente	-30.89	-71.68	CRN	5	Saillard et al., 2009	678±51 (17)
Chile	Puertecillo	-34.09	-71.94	IRSL	5	Jara-Munoz et al., 2015	87±7 (5c)
Chile	Pichilemu	-34.38	-71.97	IRSL	5	Jara-Munoz et al., 2015	106±9 (5c)
Chile	Putu	-35.16	-72.25	IRSL	5	Jara-Munoz et al., 2015	85±8 (5c)
Chile	Constitucion	-35.40	-72.49	IRSL	5	Jara-Munoz et al., 2015	105±8 (5c)
Chile	Constitucion	-35.44	-72.47	IRSL	5	Jara-Munoz et al., 2015	124±11
Chile	Carranza	-35.58	-72.61	IRSL	5	Jara-Munoz et al., 2015	67±6 (5c)
Chile	Carranza	-35.64	-72.54	IRSL	5	Jara-Munoz et al., 2015	104±9
Chile	Pelluhue	-35.80	-72.54	IRSL	5	Jara-Munoz et al., 2015	112±10
Chile	Pelluhue	-35.80	-72.55	IRSL	5	Jara-Munoz et al., 2015	102±9 (5c)
Chile	Curanipe	-35.97	-72.78	IRSL	5	Jara-Munoz et al., 2015	265±29
Chile	Arauco	-37.62	-73.67	IRSL	5	Jara-Munoz et al., 2015	89±9 (5c)
Chile	Arauco	-37.68	-73.57	CRN	5	Melnick et al., 2009	127±13
Chile	Arauco	-37.71	-73.39	CRN	5	Melnick et al., 2009	133±14
Chile	Arauco	-37.76	-73.38	CRN	5	Melnick et al., 2009	130±13
Chile	Cerro Caleta Curiñanco	-39.72	-73.40	Tephrochronology	4	Pino et al., 2002	~125
Chile	South Curiñanco	-39.76	-73.39	Tephrochronology	4	Pino et al., 2002	~125
Chile	Valdivia	-39.80	-73.39	Tephrochronology	4	Pino et al., 2002	~125
Chile	Camping Bellavista	-39.85	-73.40	Tephrochronology	4	Pino et al., 2002	~125
Chile	Mancera	-39.89	-73.39	Tephrochronology	5	Silva, 2005	~125

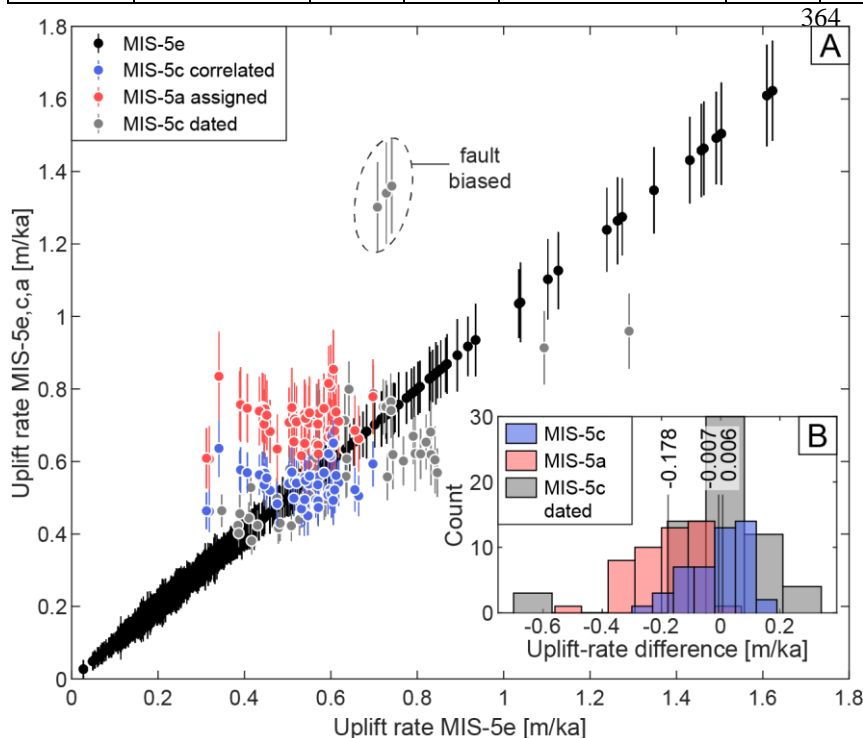


Figure 3. Comparison of MIS-5 uplift-rate estimates. (A) Uplift rates derived by correlating mapped terrace occurrences located immediately below the MIS-5e level to either MIS-5c (blue) or MIS-5a (red) with respect to MIS-5e uplift rates. Marine terraces correlated to MIS-5c by an age constraint are plotted in gray color. (B) Histograms of differences between MIS-5a or MIS-5c uplift rates and MIS-5e uplift rates. Vertical lines show median uplift-rate differences.

383 To quantify the reliability and consistency of our shoreline-angle measurements, we [developed](#) a quality rating from
 384 low (1) to high (5) confidence. [The following Equation 1 illustrates how we calculated the individual parameters and](#)
 385 [the overall quality rating:](#)

386 [Equation 1: Quality rating.](#)

$$387 \quad QR = 1 + 2.4 * \left(\frac{C_{RP}}{\max(C_{RP})} * \left(1 - \frac{D_{RP}}{\max(D_{RP})} \right) \right)^e + 1.2 * \left(1 - \frac{E_T}{\max(E_T)} \right) + 0.4 * 1.2 * \left(1 - \frac{R}{\max(R)} \right)$$

388 The four parameters that ~~are we~~ included in our quality rating (QR) comprise a) the distance to the nearest referencing
 389 point (D_{RP}), b) the confidence of the referencing point that is based on the dating method used by previous studies
 390 (C_{RP}) (Pedoja et al., 2011), c) the measurement error in TerraceM (E_T), and (d) the pixel-scale resolution of the
 391 topographic data set (R) (Fig. [34](#)). We did not include the error that results from the usage of different swath widths,
 392 since the calculated elevation difference with respect to the most frequently used 200 m swath width is very low (<
 393 0.5 m) (Fig. [2C2E](#)). From the reference points we only used data points with a confidence value of 3 or greater (1 –
 394 poor, 5 – very good) based on the previous qualification of Pedoja et al. (2011). [The confidence depends mainly on](#)
 395 [the reliability of the dating method, but can be increased by good age constraints of adjacent terrace levels or detailed](#)
 396 [morphostratigraphic correlations, such as in Chala Bay \(Fig. 2A\)](#) (Goy et al., 1992; Saillard, 2008). We further used
 397 this confidence value to quantify the quality of the age constraints in the WALIS template.

398 To account for the different uncertainties of the individual parameters in the QR, we combined and weighted the
 399 parameters D_{RP} and C_{RP} in a first equation claiming 60% of the final QR, E_T in a second and R in a third equation
 400 weighted 30% and 10%, respectively. We justify these percentages by the fact that the distance and confidence to the
 401 nearest referencing point is of utmost importance for identifying the MIS-5e terrace level. The measurement error
 402 represents how well the mapping of the paleo-platform and paleo-cliff ~~led to resulted in~~ the shoreline-angle
 403 measurement, while the topographic resolution of the underlying DEM only influences the precise representation of
 404 the actual topography and has little impact on [the](#) measurement itself. [The coefficient assigned to the topographic](#)
 405 [resolution is multiplied by a factor of 1.2 in order to maintain the possibility of a maximum QR for a DEM resolution](#)
 406 [of 5 m.](#) Furthermore, we added an exponent to the first part of the equation to reinforce low confidence and/or high
 407 distance of the referencing point for low quality ratings. [The exponent adjusts the QR according to the distribution of](#)
 408 [distances from referencing points, which follows an exponential relationship \(Fig. 4D\).](#) ~~The following equation~~
 409 ~~illustrates how we calculated the individual parameters and the overall quality rating:~~

$$410 \quad QR = 1 + 2.4 * \left(\frac{C_{RP}}{\max(C_{RP})} * \left(1 - \frac{D_{RP}}{\max(D_{RP})} \right) \right)^e + 1.2 * \left(1 - \frac{E_T}{\max(E_T)} \right) + 0.4 * 1.2 * \left(1 - \frac{R}{\max(R)} \right)$$

411 The influence of each parameter to the quality rating can be observed in Fig. [34](#). We observe that for high D_{RP} values
 412 the QR becomes constant; likewise, the influence of QR parameters becomes significant for QR values higher than 3.
 413 We justify the constancy of the QR for high D_{RP} values (> 300 km) by the fact that most terrace measurements have

414 D_{RP} values below 200 km (Fig. 3D4D). The quality rating is then used as a descriptor of the confidence of marine
 415 terrace-elevation measurements.

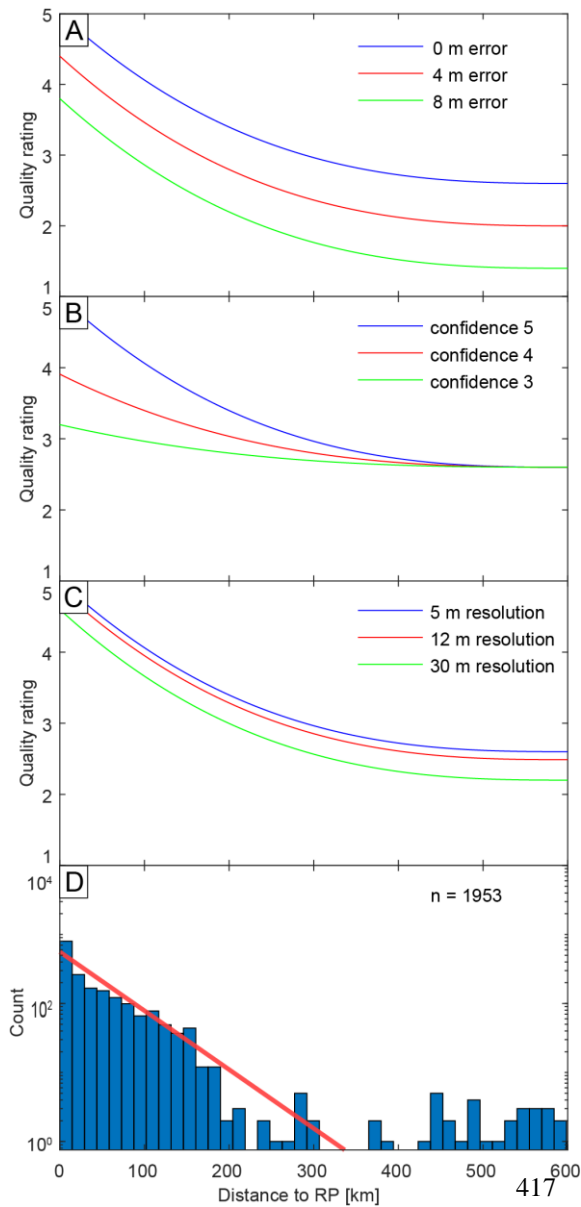


Figure 34. Influence of the parameters on the quality rating. The x -axis is the distance to reference point (RP), the y -axis is the quality rating, the color lines represent different values of quality rating parameters. While one parameter is being tested, the remaining parameters are set to their best values. That is why the QR does not reach values of 1 in the graphs displayed here. (A) Shoreline-angle elevation error. (B) Confidence value of the referencing point. (C) Topographic resolution of the DEM used for terrace-elevation estimation. (D) Histogram displaying the distribution of distances between each shoreline-angle measurement and its nearest RP (n : number of measurements). The red line is an exponential fit.

418 3.2. Estimating coastal uplift rates

419 Uplift-rate estimates from marine terraces (u) were calculated using the following equations 2 and 3:

420 [Equation 2: Relative sea level.](#)

421
$$\Delta H = H_T - H_{SL}$$

422 [Equation 3: Uplift rate.](#)

423
$$u = \frac{H_T - H_{SL}}{T}$$

424 where ΔH is the relative sea level, H_{SL} is the sea-level altitude of the interglacial maximum, H_T is the shoreline-angle
 425 elevation of the marine terrace, and T its associated age (Lajoie, 1986).

426 We calculated the standard error $SE(u)$ using ~~the following~~ equation 4 from Gallen et al. (2014):

427 Equation 4: Uplift-rate error.

428
$$SE(u)^2 = u^2 \left(\left(\frac{\sigma_{\Delta H}^2}{\Delta H^2} \right) + \left(\frac{\sigma_T^2}{T^2} \right) \right)$$

429 where $\sigma_{\Delta H}^2$, the error in relative sea level, equals $(\sigma_{H_T}^2 + \sigma_{H_{SL}}^2)$. The standard-error estimates comprise the uncertainty
 430 in shoreline-angle elevations from TerraceM (σ_{H_T}), error estimates in absolute sea level ($\sigma_{H_{SL}}$) from Rohling et al.
 431 (2009), and an arbitrary range of 10 ka for the duration of the highstand (σ_T).

432 Vertical displacement rates and relative sea level are influenced by flexural rebound associated with loading and
 433 unloading of ice sheets during glacio-isostatic adjustments (GIA) (Stewart et al., 2000; Shepherd and Wingham, 2007).
 434 The amplitude and wavelength of GIA is mostly determined by the flexural rigidity of the lithosphere (Turcotte and
 435 Schubert, 1982) and should therefore not severely influence vertical deformation along non-glaciated coastal regions
 436 (Rabassa and Clapperton, 1990) that are located in the forearc of active subduction zones. Because of their intrinsic
 437 modeling complexities, we did not account for the GIA effect on terrace elevations and uplift rates.

438 3.3. Tectonic parameters of the South American convergent margin

439 We compared the deformation patterns of marine terraces along the coast of South America with proxies that included
 440 crustal faults, bathymetric anomalies, trench-sediment thickness, and distance to the trench. To evaluate the possible
 441 control of climatic parameters in the morphology of marine terraces, we compared our data set with wave heights,
 442 tidal range, mean annual precipitation rate, and the azimuth of the coastline (Schweller et al., 1981; Bangs and Cande,
 443 1997; von Huene et al., 1997; Collot et al., 2002; Ceccherini et al., 2015; Hayes et al., 2018; Santibáñez et al., 2019;
 444 GEBCO Bathymetric Compilation Group, 2020) (Fig. 1).

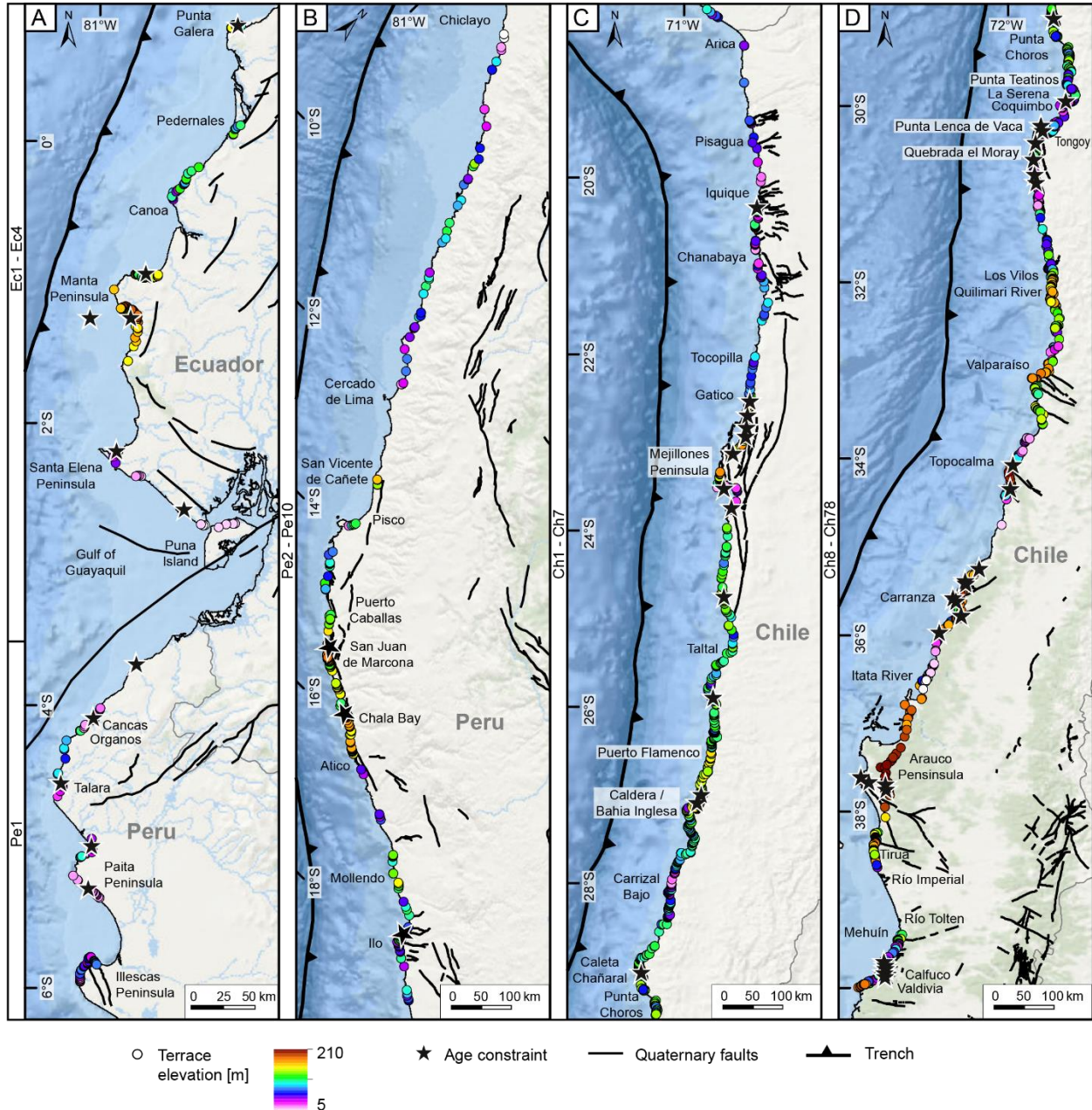
445 To evaluate the potential correlations between tectonic parameters and marine terraces, we ~~then~~ analyzed the
 446 latitudinal variability of these parameters projected along a curved “simple profile” and a 300-km-wide “swath profile”
 447 following the trace of the trench. We used simple profiles for visualizing 2D data sets; for instance, to compare crustal
 448 faults along the forearc area of the margin (Veloza et al., 2012; Melnick et al., 2020), we projected the seaward tip of
 449 each fault. For the trench-sediment thickness, we projected discrete thickness estimates based on measurements from
 450 ~~reflection~~ seismic reflection profiles of Bangs and Cande (1997), Collot et al. (2002), Huene et al. (1996), and
 451 Schweller et al. (1981). Finally, we projected the discrete trench distances from the point locations of our marine
 452 terrace measurements along a simple profile. To compare bathymetric features on the oceanic plate, we used a

453 compilation of bathymetric measurements at 450 m resolution (GEBCO Bathymetric Compilation Group, 2020). The
454 data set was projected along a curved, 300-km-wide swath profile using TopoToolbox (Schwanghart and Kuhn, 2010).
455 Finally, to elucidate the influence of climatic factors on marine terrace morphology, we compared the elevation, but
456 also the number of measurements as a proxy for preservation and exposure of marine terraces. We calculated wave
457 heights, tidal ranges, and reference water levels at the point locations of our marine terrace measurements using the
458 Indicative Meaning Calculator (IMCalc) from Lorscheid and Rovere (2019). We used the maximum values of the
459 hourly significant wave height, and for the tidal range we calculated the difference between the highest and lowest
460 astronomical tide. The reference water level represents the averaged position of the paleo sea level with respect to the
461 shoreline-angle elevation and, together with the indicative range (uncertainty), quantifies the indicative meaning
462 (Lorscheid and Rovere, 2019). We furthermore used the high-resolution data set of Ceccherini et al. (2015) for mean
463 annual precipitation, and we compared the azimuth of the coast in order to evaluate its exposure to wind and waves.
464 To facilitate these comparisons, we extracted the values of all these parameters at the point locations of our marine
465 terrace measurements and projected them along a simple profile. Calculations and outputs were processed and
466 elaborated using MATLAB® 2020b.

467 **4. Results**

468 **4.1. Marine terrace geomorphology and shoreline-angle elevations**

469 In the following sections we describe our synthesized database of last interglacial marine terrace elevations along the
470 WSAC. Marine terraces of the last interglacial are generally well preserved and almost continuously exposed along
471 the WSAC, allowing to estimate elevations with a high spatial density. To facilitate the descriptions of marine terrace-
472 elevation patterns, we divided the coastline into four sectors based on their main morphometric-geomorphic
473 characteristics (Fig. 45): 1) the Talara bend in northern Peru and Ecuador, 2) southern and central Peru, 3) northern
474 Chile, and 4) central and south-central Chile. In total we carried out 1,843 MIS-5e terrace measurements with a median
475 elevation of 30.1 m asl and 110 MIS-5c terrace measurements with a median of 38.6 m. The regions with exceptionally
476 high marine terrace elevations (≥ 100 m) comprise the Manta Peninsula in Ecuador, the San Juan de Marcona area in
477 south-central Peru, and three regions in south-central Chile (Topocalma, Carranza, and Arauco). Marine terraces at
478 high altitudes (≥ 60 m) can also be found in Chile on the Mejillones Peninsula, south of Los Vilos, near Valparaíso,
479 in Tirua, and near Valdivia, while terrace levels only slightly above the median elevation are located at Punta Galera
480 in Ecuador, south of Puerto Flamenco, at Caldera/Bahía Inglesa, near Caleta Chañaral, and near the Quebrada El
481 Moray in the Altos de Talinay area in Chile. In the next-following sections we described the characteristics of each
482 site in detail, the names of the sites are written in brackets following the same nomenclature as in the WALIS database
483 (i.e., Pe – Peru, Ec – Ecuador, Ch – Chile).



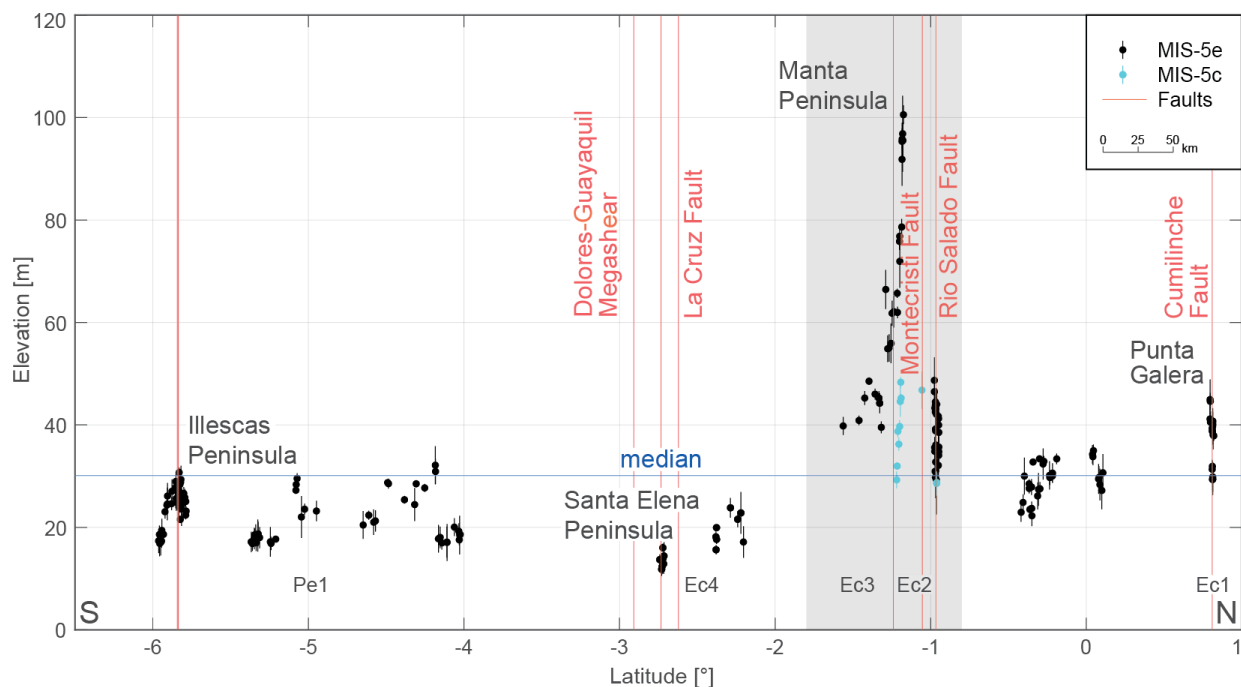
484

485 **Figure 45.** Shoreline-angle elevation measurements (colored points), referencing points (black stars), Quaternary faults
 486 (bold black lines) (Veloza et al., 2012; Melnick et al., 2020), and locations mentioned in the text for the four main
 487 **morphometric-geomorphic** segments (for location see Fig. 1A) (World Ocean Basemap: Esri, Garmin, GEBCO, NOAA
 488 NGDC, and other contributors). **Site names referring to the entries in the WALIS database are on the left margin of each**
 489 **sub-figure (Pe – Peru, Ec – Ecuador, Ch – Chile).** (A) Talara bend in Ecuador and northern Peru. (B) Central and southern
 490 Peru. (C) Northern Chile. (D) Central and south-central Chile.

491 **4.1.1. Ecuador and northern Peru (1°N–6.5°S)**

492 The MIS-5e terrace levels in Ecuador and northern Peru [sites Ec1 to Ec4 and Pe1] are discontinuously preserved
 493 along the coast (Fig. 56). They often occur at low elevations (between 12 m and 30 m) and show abrupt local changes

494 in elevation, reaching a maximum at the Manta Peninsula. Punta Galera in northern Ecuador displays relatively broad
 495 and well-preserved marine terraces ranging between 40 and 45 m elevation and rapidly decreasing eastward to ~~around~~
 496 ~~about~~ 30 m asl across the Cumilínche fault [Ec1]. Farther south, between Pedernales and Canoa [Ec1], narrow terraces
 497 occur at lower altitudes of 22–34 m asl. A long-wavelength (~120 km) pattern in terrace-elevation change can be
 498 observed across the Manta Peninsula with the highest MIS-5e terraces peaking at ~100 m asl at its southern coast
 499 [Ec2]. This terrace level is hardly visible in its highest areas with platform widths smaller than 100 m due to deeply
 500 incised and narrowly spaced river valleys. We observe lower and variable elevations between 30 and 50 m across the
 501 Rio Salado fault in the San Mateo paleo-gulf in the north, while the terrace elevations increase gradually from ~40 m
 502 in the Pile paleo-gulf in the south [Ec3] toward the center of the peninsula (El Aromo dome) and the Montecristi fault
 503 [Ec3]. A lower terrace level correlated to MIS-5c displays similar elevation patterns as MIS-5e within the Pile paleo-
 504 gulf and ~~northward-areas to the north~~. Near the Gulf of Guayaquil and the Dolores-Guayaquil megashear, the lowest
 505 terrace elevations occur at the Santa Elena Peninsula ranging between 17 and 24 m asl and even lower altitudes in its
 506 southern part, and on the Puna Island ranging between 11 and 16 m asl [Ec4]. In northern Peru [Pe1], we observe
 507 dismembered MIS-5e terraces in the coastal area between Cancas and Talara below the prominent Mancora Tablazo.
 508 “Tablazo” is a local descriptive name used in northern Peru (~3.5–6.5°S) for marine terraces that cover a particularly
 509 wide surface area (Pedoja et al., 2006b). South of Cancas, MIS-5e terrace elevations range between 17 and 20 m asl,
 510 reaching 32 m near Organos, and vary between 20 and 29 m in the vicinity of Talara. In the southward continuation
 511 of the Talara harbor, the Talara Tablazo widens, with a lower marine terrace at ~~around-about~~ 23 m asl immediately
 512 north of Paita Peninsula reaching 30 m asl in the northern part of the peninsula. The last occurrence of well-preserved
 513 MIS-5e terraces in this sector ~~is-exists~~ at the Illescas Peninsula, where terrace elevations decrease from around 30 m
 514 to 17 m asl southward.



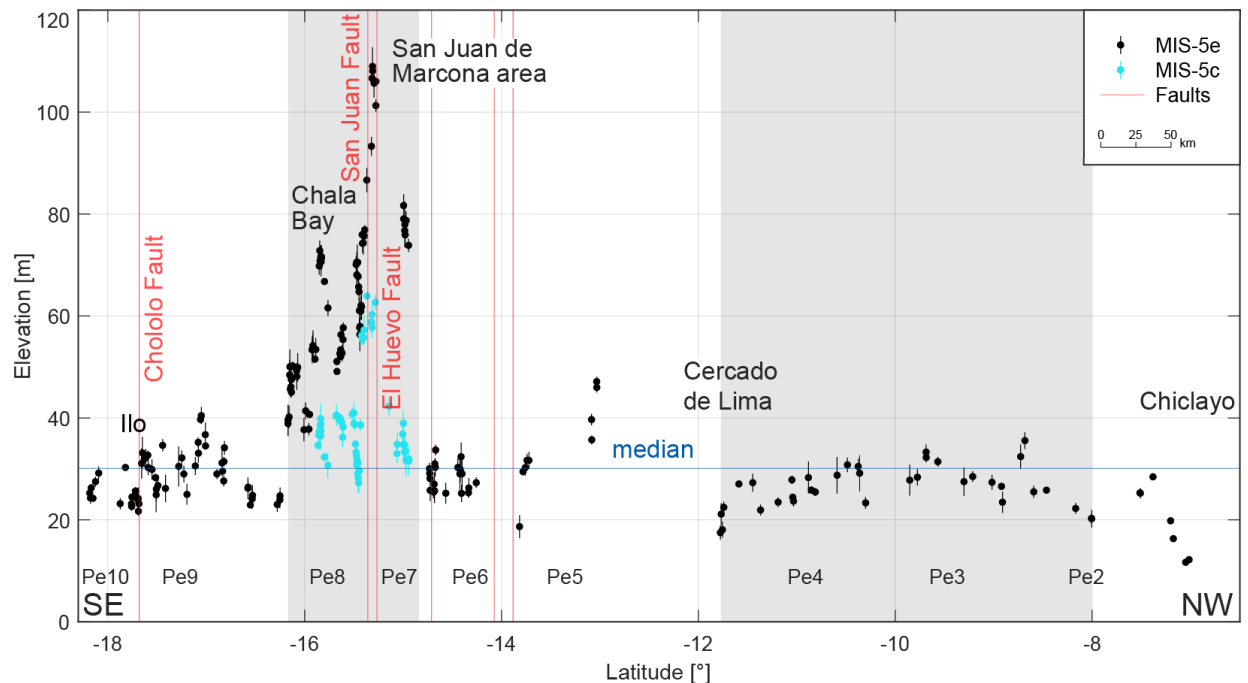
515 **Figure 56.** Measured shoreline-angle elevations of MIS-5e and 5c in Ecuador (Ec) and northern Peru (Pe). A high and
 516 inferred long-wavelength change in terrace elevation occurs at the Manta Peninsula (gray area) and ~~quite-at~~ low altitudes
 517

518 [elevations](#) farther south at the Santa Elena Peninsula. Several [short-scale terrace-elevation changes over short distances](#)
519 [coincide with faulting at Punta Galera and on the Illescas Peninsula. Median elevation: 30.1 m. For location see Fig. 4A5A.](#)

520 4.1.2. Central and southern Peru (6.5°–18.3°S)

521 This segment comprises marine terraces at relatively low and constant elevations, but which are rather discontinuous
522 [sites Pe2 to Pe10], except in the San Juan de Marcona area, where the terraces increase in elevation drastically (Fig.
523 [67](#)). The coast in north-central Peru exhibits poor records of MIS-5e marine terraces, characterized by mostly narrow
524 and discontinuous remnants that are sparsely distributed along the margin [with limited age constraints](#). Marine terraces
525 increase in elevation from 11 to 35 m asl south of Chiclayo [Pe2] and decrease to 17 m asl near Cercado de Lima [Pe3,
526 Pe4], forming a long-wavelength (~600 km), small amplitude (~20 m) upwarped structure. The MIS-5e terrace levels
527 are better expressed in the south-central and southern part of Peru at elevations between 35 and 47 m asl in San Vicente
528 de Cañete, decreasing to approximately 30 m asl in the vicinity of Pisco [Pe5]. South of Pisco, the coastal area becomes
529 narrow with terrace elevations ranging between 25 and 34 m asl [Pe6] and increasing abruptly to 74–79 m near Puerto
530 Caballas and the Río Grande delta. MIS-5e terrace elevations are highest within the San Juan de Marcona area,
531 reaching 109–93 m at Cerro Huevo and 87–56 m at Cerro Trés Hermanas [Pe7]. These higher terrace elevations
532 coincide with a wider coastal area, a better-preserved terrace sequence, and several crustal faults, such as the San Juan
533 and El Huevo faults.

534 Terrace heights west of Yauca indicate a further decrease to 50–58 m before a renewed increase to 70–72 m can be
535 observed in the Chala embayment [Pe8]. We observe a similar trend in elevation changes for the shoreline angles
536 attributed to the MIS-5c interglacial within the previously described high-elevation area: 31–39 m near the Río Grande
537 delta, 62–58 m below the Cerro Huevo peak, 64–27 m below the Cerro Trés Hermanas peak [Pe7], 36–40 m near
538 Yauca, and 34–40 m within the Chala embayment [Pe8]. Besides various changes in between, terrace elevations
539 decrease slowly from 54 m south of the Chala region to 38 m near Atico [Pe8]. The overall decrease south of the San
540 Juan de Marcona area therefore contrasts strikingly with the sharper decrease to the north. These high-elevation marine
541 terraces, which extend ~250 km along the coast from north of the San Juan de Marcona area to south of Chala Bay,
542 constitute one of the longest wavelength structures of the WSAC. Southeast of Atico, less well-preserved marine
543 terraces appear again in form of small remnants in a narrower coastal area. Starting with elevations as low as 24 m,
544 MIS-5e terrace altitudes increase southeastward to up to 40 m near Mollendo [Pe9], before they slightly decrease
545 again. The broader and quite well-preserved terraces of the adjacent Ilo area resulted in a smooth increase from values
546 greater than 25 m to 33 m and a sudden decrease to as low as 22 m across the Chololo fault [Pe9]. North of the Arica
547 bend, shoreline-angle measurements yielded estimates of 24–29 m in altitude [Pe10].

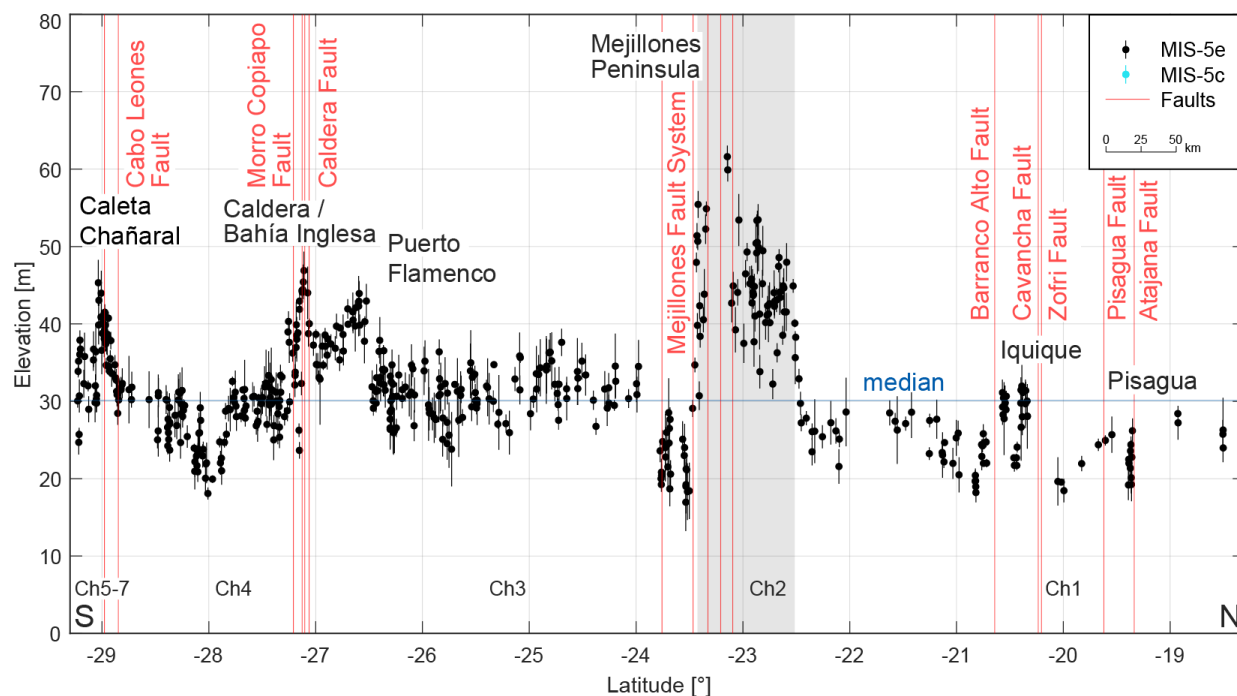


548
 549 **Figure 67.** Measured shoreline-angle elevations of MIS-5e and 5c terraces in central and southern Peru (Pe). While only
 550 sparsely preserved terraces below the median (30.1 m) occur in central Peru between Chiclayo and Lima, a relatively broad
 551 and asymmetric distribution of marine terraces characterizes the area of San Juan de Marcona. For location see Fig. 4B5B.

552 **4.1.3. Northern Chile (18.3°–29.3°S)**

553 Along the northern Chilean coast, marine terraces of the MIS-5e are characterized by a variable elevation pattern and
 554 the occurrence of numerous crustal faults associated with the Atacama fault system, although the changes in terrace
 555 elevation are not as pronounced as in the northern segments (Fig. 78) [sites Ch1 to Ch7]. The local widening of the
 556 coastal area near the Arica bend narrows southward with MIS-5e terraces at elevations of between 24 and 28 m asl in
 557 northernmost Chile [Ch1]. Just north of Pisagua, we measured shoreline-angle elevations of well-preserved marine
 558 terraces between 19 and 26 m across the Atajana fault [Ch1]. A short-scale An areally limited zigzag pattern starting
 559 with shoreline-angle elevation values of 32 m south of Iquique and south of the Zofri and Cavanca faults decreases
 560 rapidly to approximately 22 m, but increases again to similar altitudes and drops as low as 18 m toward Chanabaya
 561 south of the Barranco Alto fault [Ch1]. A gentle, steady rise in terrace elevations can be observed south of Tocopilla
 562 where altitudes of 25 m are attained. South of Gatico, terrace markers of the MIS-5e highstand increase and continue
 563 northward for much of the Mejillones Peninsula within an approximate elevation range of 32–50 m asl, before reaching
 564 a maximum of 62 m asl at the Pampa de Mejillones [Ch2]. With its ~100 km latitudinal extent, we consider this
 565 terrace-elevation change to be a medium-wavelength structure. Although no MIS-5e terrace levels have been
 566 preserved at the Morro Mejillones Horst (Binnie et al., 2016), we measured shoreline-angle elevations at the elevated
 567 southwestern part of the peninsula that decrease sharply from 55 to 17 m asl in the vicinity of the Mejillones fault
 568 system [Ch2]. After a short discontinuation-interruption of the MIS-5e terrace level at Pampa Aeropuerto, elevations
 569 remain relatively low between 19–25 m farther south [Ch2]. Along the ~300-km coastal stretch south of Mejillones,
 570 marine terraces are scattered along the narrow coastal area ranging between 25 and 37 m asl [Ch3]. South of Puerto

571 Flamenco, MIS-5e terrace elevations range between 40 and 45 m asl until Caldera and Bahía Inglesa [Ch4]. The MIS-
 572 5e marine terrace elevations decrease abruptly south of the Caldera fault and the Morro Copiapó (Morro Copiapó
 573 fault) to between 25 and 33 m asl, reaching 20 m asl north of Carrizal Bajo [Ch4]. In the southernmost part of the
 574 northern Chilean sector, the MIS-5e terraces rise from around 30 m asl to a maximum of 45 m asl near the Cabo
 575 Leones fault [Ch4], before ~~declining~~ decreasing in elevation abruptly near Caleta Chañaral and Punta Choros [Ch5,
 576 Ch6, Ch7].

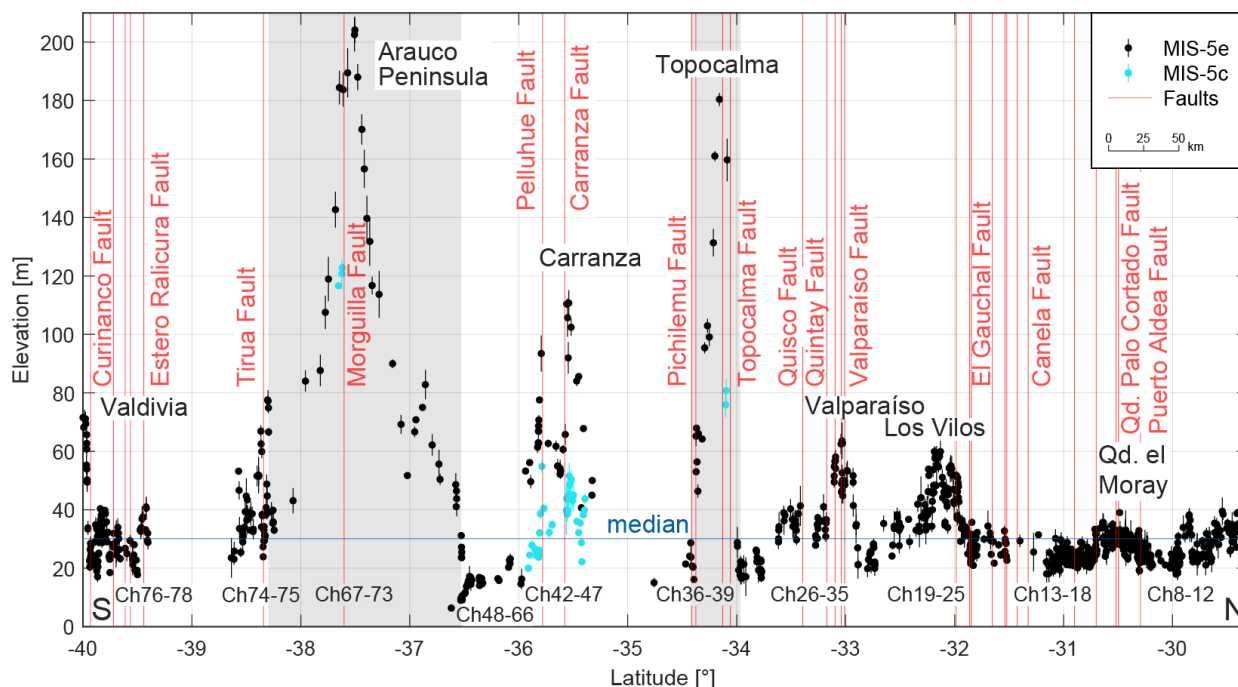


577 **Figure 78.** Measured shoreline-angle elevations of MIS-5e and 5c terraces in northern Chile (**Ch**). Faults as well as and
 578 asymmetrically uplifted marine terraces of up to 60 m elevation characterize the Mejillones Peninsula, reaching values
 579 below 20 m at the southern margin. Terrace elevations attain peak values south of Puerto Flamenco, at Caldera/Bahía
 580 Inglesa, and north of Caleta Chañaral, while in between minimum altitudes elevations below 20 m ~~occur~~ prevail (north of
 581 Carrizal Bajo). Median elevation is 30.1 m. For location see Fig. ~~4C5C~~.
 582

583 4.1.4. Central Chile (29.3°–40°S)

584 Marine terraces along central Chile display variable, high-amplitude terrace-elevation patterns associated with
 585 numerous crustal faults, and include a broad-scale change in terrace altitudes with the highest MIS-5e marine terrace
 586 elevations of the entire South American margin on the Arauco Peninsula (Fig. 89) [sites Ch8 to Ch78]. South of Punta
 587 Choros, marine terrace elevations decrease from values close to 40 to 22 m asl north of Punta Teatinos [Ch8, Ch9]. A
 588 maximum elevation of 40 m is reached by the terraces just south of this area [Ch10] whereas north of La Serena, a
 589 sharp decrease leads to values between 20 and 30 m for marine terraces south of Coquimbo Bay and in the Tongoy
 590 Bay area [Ch11, Ch12]. South of Punta Lengua de Vaca, our measurements of the exceptionally well-preserved
 591 staircase morphology of the terraces are within the same elevation range between 20 and 30 m, increasing slowly to
 592 40 m near the Quebrada el Moray [Ch13]. Although we could not observe a significant change in terrace elevation
 593 across the Puerto Aldea fault, we measured an offset of ~7 m across the Quebrada Palo Cortado fault. MIS-5e terrace
 594 levels decrease thereafter and vary between 20 and 30 m in altitude until north of Los Vilos [Ch14–Ch18], where they

595 increase in elevation [Ch19], reaching 60 m near the Río Quilimari [Ch20]. The marine terraces become wider in this
 596 area and are associated with scattered sea stacks. Decreasing farther south to only 20 m asl [Ch21–Ch25], the coastal
 597 area narrows and has terrace heights of up to 64 m near Valparaíso. in an area that ~~are~~ is cut by numerous faults (e.g.,
 598 Valparaíso and Quintay faults) [Ch26–Ch32]. Another low-elevation area follows southward, with values as low as
 599 17 m [Ch33–Ch35]. Farther south, between 34°S and 38°S, broad (~200 km at Arauco), medium (~45 km at
 600 Topocalma), and narrow (Carranza) upwarped zones occur that are manifested by variable terrace elevations. These
 601 include prominent high-terrace elevations at Topocalma with a maximum of 180 m [Ch36–Ch39], slightly lower levels
 602 of 110 m at Carranza [Ch42–Ch47], exceptionally low values near the Río Itata (< 10 m) [Ch48–Ch64, Ch66], and
 603 the most extensive and highest shoreline-angle elevations on the Arauco Peninsula with elevations in excess of 200 m
 604 [Ch67–Ch73]. Additionally, we measured MIS-5c terrace elevations in the three higher exposed areas with a range of
 605 20–55 m at Carranza, and a few locations at Topocalma (76–81 m) and Arauco (117–123 m). The medium-wavelength
 606 structure of Topocalma is bounded by the Pichilemu and Topocalma faults, and near Carranza several fault offsets
 607 (e.g., Pelluhue and Carranza faults) are responsible for the short-wavelength changes in terrace elevation. In contrast,
 608 crustal faulting is nearly absent in the high-elevation and long-wavelength structure at Arauco. MIS-5e terrace
 609 elevations are highly variable within a short area south of the Arauco Peninsula near the Tirua fault, increasing rapidly
 610 from 27 m to 78 m and decreasing thereafter to ~~around~~ approximately 20 m [Ch74, Ch75]. The continuity of terraces
 611 is interrupted by the absence of terrace levels between Río Imperial and Río Toltén, but resumes afterward with a
 612 highly frequent zigzag pattern and multiple faults (e.g., Estero Ralicura and Curinanco faults) from as low as 18 m to
 613 a maximum of 40 m [Ch76, Ch77]. In this area locations with the highest terrace levels comprise the terraces near
 614 Mehuín and Calfuco. A final increase in shoreline-angle elevations from ~~around~~ about 20–30 m up to 76 m near
 615 Valdivia coincides with the southern terminus of our terrace-elevation measurements [Ch78].



616
 617 **Figure 89.** Measured shoreline-angle elevations of MIS-5e and 5c terraces in central Chile (Ch). Extensive faulting coincides
 618 with various high terrace elevations of the last interglacial highstand north of Los Vilos, near Valparaíso, at Topocalma,

619 Carranza, and near Valdivia. The most pronounced and long-wavelength change in terrace elevation occurs on the Arauco
620 Peninsula with maximum elevations over 200 m and minimum elevations below 10 m north of Concepción. [Qd. – Quebrada.](#)
621 Median elevation: 30.1 m. For location see Fig. [4D5D](#).

622 4.2. Statistical analysis

623 Our statistical analysis of mapped shoreline-angle elevations resulted in a maximum kernel density at 28.96 m with a
624 95% confidence interval from 18.59 m to 67.85 m (2σ) for the MIS-5e terrace level (Fig. [9A10A](#)). The MIS-5c terrace
625 yielded in a maximum kernel density at a higher elevation of 37.20 m with 2σ ranging from 24.50 m to 63.92 m. It is
626 important to note that the number of MIS-5c measurements is neither as high nor as continuous as compared to that
627 of the MIS-5e level. MIS-5c data points were measured almost exclusively in sites where MIS-5e reach high elevations
628 (e.g., San Juan de Marcona with MIS-5e elevations between 40 and 110 m).

629 The distribution of measurement errors was studied using probability kernel-density plots for each topographic
630 resolution (1-5 m LIDAR, 12 m TanDEM-X, and 30 m TanDEM-X). The three data sets display similar distributions
631 and maximum likelihood probabilities (MLP); for instance, LiDAR data show a MLP of 0.93 m, the 12 m TanDEM-
632 X a MLP of 1.16 m, and 30 m TanDEM-X a MLP of 0.91 m (Fig. [9B10B](#)). We observe the lowest errors from the 30
633 m TanDEM-X, slightly higher errors from the 1-5 m LiDAR data, and the highest errors from the 12 m TanDEM-X.
634 This observation is counterintuitive as we would expect lower errors for topographic data sets with higher resolution
635 [\(1-5 m LiDAR\)](#). The reason for these errors is probably related to the higher number of measurements using the 12 m
636 TanDEM-X (1564) in comparison with the measurements using 30 m TanDEM-X (50), which result in a higher
637 dispersion [and a more realistic representation of the measurement errors](#) (Fig. [9B10B](#)). In addition, the relation
638 between terrace elevations and error estimates shows that comparatively higher errors are associated with higher
639 terrace elevations, although the sparse point density of high terrace-elevation measurements prevents a clear
640 correlation from being recognized (Fig. [9C10C](#)).

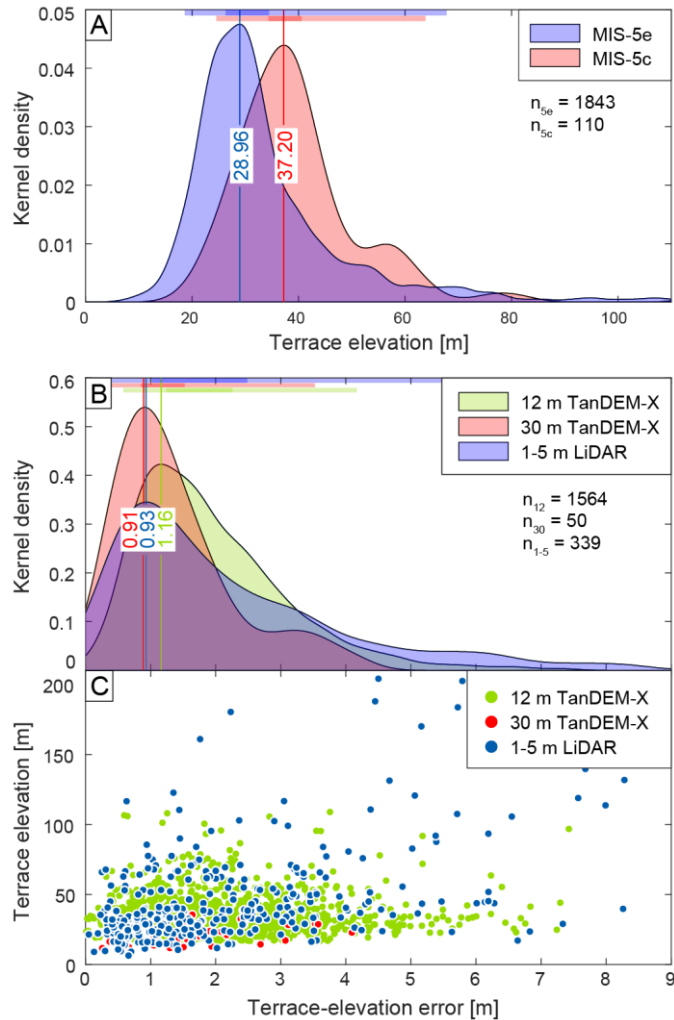


Figure 910. Statistical analysis of measured shoreline-angle elevations. (A) Kernel-density plot of MIS-5e and 5c terrace elevations with maximum likelihood probabilities (MLP_{m.l.p.}) at 28.96 m elevation for MIS-5e and 37.20 m elevation for MIS-5c (n : number of measurements). Colored bars on top highlight the standard deviations σ and 2σ . (B) Kernel-density and their associated standard-deviation (σ and 2σ) calculations of terrace-elevation errors for source DEMs of various resolutions. The most abundant 12 m TanDEM-X has a MLP_{m.l.p.}-error of 1.16 m, while the 30 m TanDEM-X and the 1-5 m LIDAR produce slightly lower errors of 0.91 m and 0.93 m, respectively. (C) Terrace-elevation errors plotted against terrace elevation for the individual source DEMs. Although the point density for high terrace elevations is low, a weak correlation of high errors with high terrace elevations can be observed.

641 4.3. Coastal uplift-rate estimates

642 We calculated uplift rates from 1953 terrace-elevation measurements of MIS-5e (1843) and MIS-5c (110) along the
 643 [South American margin WSAC](#) with a median uplift rate of approximately 0.22 m/ka (Fig. 4011). As with the
 644 distribution of terrace elevations, we similarly observed several [short-small](#)-scale and [long-large](#)-scale, high-amplitude
 645 changes in uplift rate along the coast. The most pronounced long-wavelength highs ($\geq 1^\circ$ latitude) in uplift rate are
 646 located on the Manta Peninsula (0.79 m/ka), in the San Juan de Marcona area (0.85 m/ka), and on the Arauco Peninsula
 647 (1.62 m/ka). Medium-wavelength structures include the Mejillones Peninsula (0.47 m/ka) and Topocalma (1.43 m/ka),
 648 while shorter wavelength structures that are characterized by exceptionally high uplift rates seem to be limited to the
 649 central Chilean part of the coastline, especially between 31.5° and 40° S. The most striking example includes Carranza
 650 with an uplift rate of up to 0.87 m/ka since the formation of the oldest MIS-5 terrace levels. Lower, but still quite high,
 651 uplift rates were calculated for areas north of Los Vilos (0.46 m/ka), near Valparaíso (0.49 m/ka), and near Valdivia
 652 (0.59 m/ka). The lowest uplift rates along the South American margin occur at Penco immediately north of Concepción

653 (0.03 m/ka), south of Chiclayo in northern Peru (0.07 m/ka), and on the southern Santa Elena Peninsula in Ecuador
654 (0.07 m/ka).

655 5. Discussion

656 5.1. Advantages and limitations of the database of last interglacial marine terrace elevations along the 657 WSAC

658 In this study we generated a systematic database of last interglacial marine terrace elevations with unprecedented
659 resolution based on an almost continuous mapping of ~2,000 measurements along 5,000 km of the WSAC. This opens
660 up several possibilities for future applications in which this database can be used; for example, ~~the fact that~~ marine
661 terraces are excellent strain markers ~~that can be~~ used in studies on deformation processes at regional scale, ~~and thus~~
662 ~~the synthesis allows~~ comparisons between deformation rates at different temporal scales ~~in different sectors of the~~
663 ~~margin~~ or analyses linking specific climate-driven ~~and tectonics~~ coastal processes, ~~and~~ landscape evolution ~~and~~
664 ~~tectonics~~. However, there are a number of limitations and potential uncertainties that can ~~affect-limit~~ the use of this
665 database in such studies without taking several caveats into consideration.

666 One of the most critical limitations of using the database is associated with the referencing points used to tie our
667 marine terrace measurements, which are in turn based on the results and chronological constraints provided by
668 previous studies. The referencing points are heterogeneously distributed along the WSAC, resulting in some cases of
669 up to 600 km distance to the nearest constrained point, such as in Central Peru [e.g. Pe2]. This may have a strong
670 influence on the confidence in the measurement of the marine terrace elevation at these sites. In addition, the
671 geochronological control of some of the referencing points may be based on dating methods with pronounced
672 uncertainties (e.g., amino acid racemization, electron spin resonance, ~~terrestrial~~ cosmogenic radionuclides), which
673 may result in equivocal interpretations and chronologies of marine terrace levels. In order to address these potential
674 factors of uncertainty we defined a quality rating (see section 3.1.), which allows classifying our mapping results based
675 on their confidence and reliability. Therefore, by considering measurements above a defined quality it is possible to
676 increase the ~~confidence~~ level of ~~confidence for~~ future studies using this database; however, this might result in a
677 decrease of the number of measurement ~~points~~ available for analysis and comparison.

678 5.2. Tectonic and climatic controls on the elevation and morphology of marine terraces along the WSAC

679 In this section we provide a brief synthesis of our data set and its implications for coastal processes and overall
680 landscape evolution ~~that are driven-influenced~~ by a combination of tectonic and climatic ~~characteristics forcing factors~~.
681 This synthesis emphasizes the significance of our comprehensive data set for a variety of coastal research problems
682 that were briefly introduced in section 5.1. Our detailed measurements of marine terraces along the WSACS reveal
683 variable elevations and a heterogeneous distribution of uplift rates associated with patterns of short-, medium-, and
684 long-wavelengths. In addition, we observe different degrees of development of marine terraces along the margin

685 expressed in variable shoreline-angle density. There are several possible causes for this variability, which we explore
686 by comparing terrace-elevation patterns with different climatic and tectonic parameters.

687 **5.2.1. Tectonic controls on coastal uplift rates**

688 The spatial distribution of the MIS-5 marine terrace elevations along the convergent South American margin has
689 revealed several high-amplitude and long-wavelength changes with respect to tectonically controlled topography.
690 Long-wavelength patterns in terrace elevation ($\sim 10^2$ km) are observed at the Manta Peninsula in Ecuador, central Peru
691 between Chiclayo and Lima, San Juan de Marcona (Peru), and on the Arauco Peninsula in Chile, while medium-
692 wavelength structures occur at Mejillones Peninsula and Topocalma (Chile). Instead, short-wavelength patterns in
693 MIS-5 terrace elevations are observed, for instance, near Los Vilos, Valparaíso, and Carranza in Chile.

694 The subduction of bathymetric anomalies has been shown to exert a substantial influence on upper-plate deformation
695 (Fryer and Smoot, 1985; Taylor et al., 1987; Macharé and Ortlieb, 1992; Cloos and Shreve, 1996; Gardner et al., 2013;
696 Wang and Bilek, 2014; Ruh et al., 2016), resulting in temporally and spatially variable fault activity, kinematics, and
697 deformation rates (Mann et al., 1998; Saillard et al., 2011; Morgan and Bangs, 2017; Melnick et al., 2019). When
698 comparing the uplift pattern of MIS-5 marine terraces and the bathymetry of the oceanic plate, we observe that the
699 two long-wavelength structures in this area, on the Manta Peninsula and ~~in the at~~ San Juan de Marcona, both coincide
700 with the location of the subducting Nazca and Carnegie ridges, respectively (Fig. ~~40A11A~~ and B); this was also
701 previously observed by other authors (Macharé and Ortlieb, 1992; Gutscher et al., 1999; Pedoja et al., 2006a; Saillard
702 et al., 2011). In summary, long-wavelength structures ~~at the coast in coastal areas of the upper plate~~ may be associated
703 with deep-seated processes (Melosh and Raefsky, 1980; Watts and Daly, 1981) possibly related to changes in the
704 mechanical behavior of the plate interface. In this context it is interesting that the high uplift rates on the Arauco
705 Peninsula do not correlate with bathymetric anomalies, which may suggest a different deformation mechanism. The
706 scarcity of crustal faults described in the Arauco area rather suggests that shallow structures associated with crustal
707 bending and splay-faults occasionally breaching through the upper crust (Melnick et al., 2012; Jara-Muñoz et al.,
708 2015; Jara-Muñoz et al., 2017; Melnick et al., 2019) ~~may~~ cause long-wavelength warping and uplift there (Fig.
709 ~~40A11A~~).

710 In contrast, small-scale bathymetric anomalies correlate in part with the presence of crustal faults perpendicular to the
711 coastal margin near, for instance, the Juan Fernandez, Taltal, and Copiapó ridges (Fig. ~~40B11B~~), ~~which; this results~~
712 in ~~short-short~~-wavelength structures and a more localized ~~altitudinal~~ differentiation of uplifted terraces. This
713 emphasizes also the importance of last interglacial marine terraces ~~as strain markers~~ with respect to currently active
714 faults, which might be compared in the future with short-term deformation estimates from GPS or the earthquake
715 catalog. In summary, short-wavelength structures ~~in the coastal realms of western South America~~ may be associated
716 with ~~erustal~~-faults that root at shallower depths within the ~~continental~~ crust (Jara-Muñoz et al., 2015; Jara-Muñoz et
717 al., 2017; Melnick et al., 2019).

718 The thickness of sediment in the trench is an additional controlling factor on forearc architecture that may determine
719 which areas of the continental margin are subjected to subduction erosion or accretion (Hilde, 1983; Cloos and Shreve,

1988; Menant et al., 2020). Our data shows that the accretionary part of the WSAC (south of the intersection with the Juan Fernandez Ridge at 32.9°S) displays faster median uplift rates of 0.26 m/ka than in the rest of the WSAC (Fig. 40B11B and C). However, no clear correlation is observed between trench fill, uplift rates, and the different structural patterns in the erosive part of the margin. On the other hand, we observe lower uplift rates for greater distances from the trench at the Arica bend, in central Peru, and in the Gulf of Guayaquil, while higher uplift rates occur in areas closer to the trench, such as near the Nazca and Carnegie ridges and the Mejillones Peninsula.

5.2.2. Climatic controls on the formation and preservation of last interglacial marine terraces

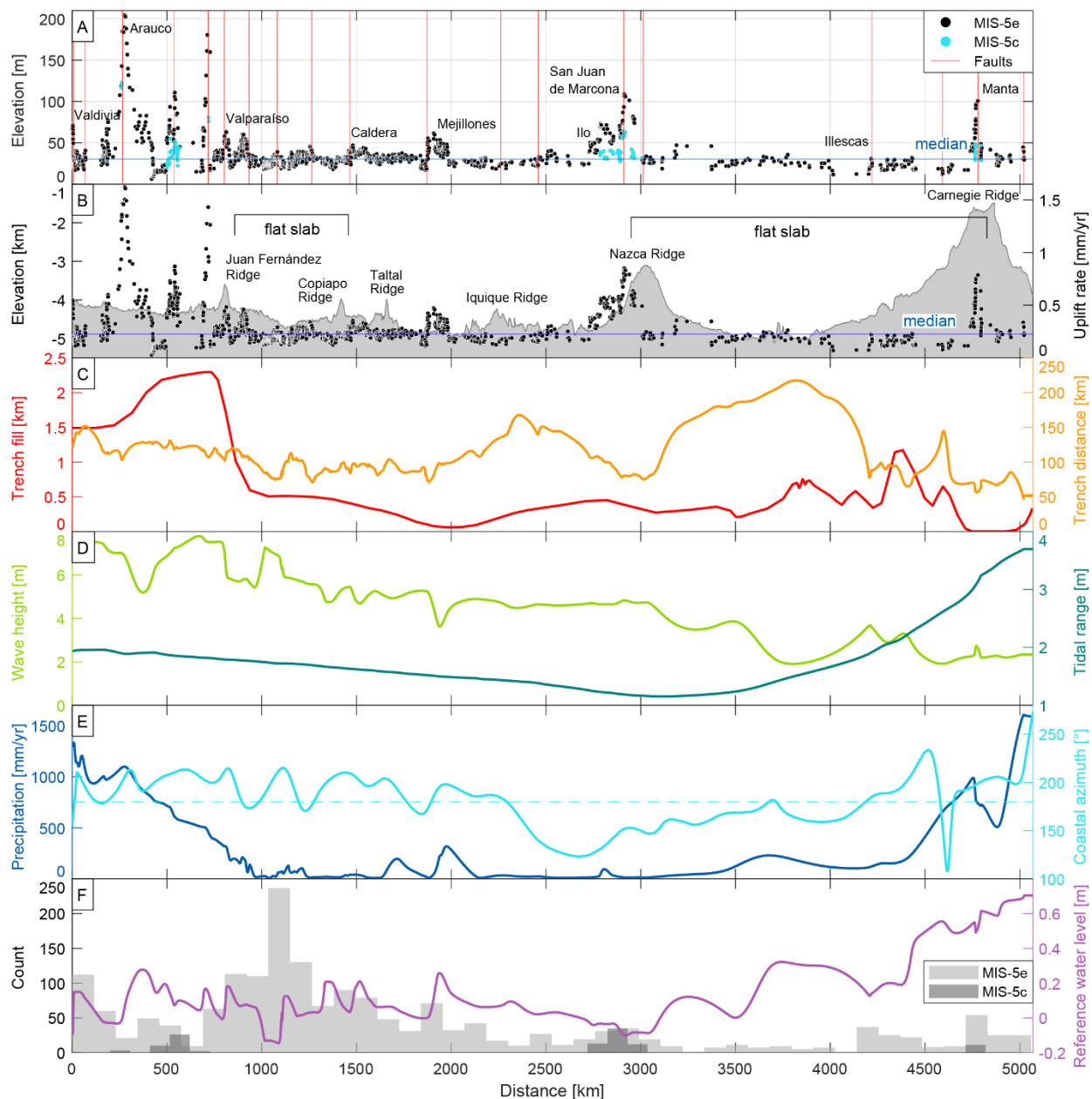
The latitudinal climate differences that characterize the western margin of South America may also control coastal morphology and the generation and preservation of marine terraces (Martinod et al., 2016b). In order to evaluate the influence of climate in the generation and/or degradation of marine terraces, we compared the number of marine terrace measurements, which is a proxy for the degree of marine terrace preservation, and climatically controlled parameters such as wave height, tidal range, coastline orientation, and the amount of precipitation.

The maximum wave height along the ~~coast of South America~~ WSAC decreases northward from ~8 to ~2 m (see section 3.3, Fig. 40D11D). Similarly, the tidal range decreases progressively northward from 2 to 1 m between Valdivia and San Juan de Marcona, followed by a rapid increase to 4 m between San Juan de Marcona and the Manta Peninsula. We observe an apparent correlation between the number of measurements and the tidal range in the north, between Illescas and Manta (Fig. 40E11F). Likewise, the increasing trend in the number of measurements southward matches with the increase in wave height (Fig. 40D11D). An increase of wave height and tidal range may lead to enhanced erosion and morphologically well-expressed marine terraces (Anderson et al., 1999; Trenhaile, 2002), which is consequently reflected in a higher number of measurements ~~that can be carried out~~. Furthermore, we observe low values for the reference water level (< 0.7 m) resulting from tide and wave-height estimations in IMCalc (Lorscheid and Rovere, 2019), which are used to correct our shoreline-angle measurements ~~in the WALIS database~~ (see section 3.3.).

The control of wave-erosion processes on the morphological expression of marine terraces may be counteracted by erosional processes such as river incision. We note that the high number of preserved marine terraces between Mejillones and Valparaíso decreases southward, which coincides with a sharp increase in mean annual precipitation from 10 to 1000 mm/yr (Fig. 40E11E and F) ~~and fluvial dissection~~. However, in the area with a high number of measurement ~~points~~ between the Illescas Peninsula and Manta we observe an opposite correlation: higher rainfall associated with an increase of marine terrace preservation (Fig. 40E11E). This ~~anticorrelation~~ suggests that the interplay between marine terrace generation and degradation processes apparently buffer each other, resulting in different responses under different climatic conditions and coastal settings.

The higher number of marine terraces between Mejillones and Valparaíso and north of Illescas corresponds with a SSW-NNE orientation of the coastline (azimuth between 200 and 220°). In contrast, NW-SE to N-S oriented coastlines (azimuth between 125 and 180°), such as between the Arica and Huancabamba bends, correlate with a lower number of marine terrace measurements (Fig. 40E11E and F). This observation ~~is~~ ~~appears~~, however, ~~counterintuitive~~

755 [implausible](#) considering that NW-SE oriented coastlines may be exposed more directly to the erosive effect of storm
 756 waves associated with winds approaching from the south. We interpret the orientation of the coastline therefore to be
 757 of secondary importance at regional scale for the formation of marine terraces compared to other parameters, such as
 758 wave height, tidal range, or rainfall.



759 **Figure 1011.** Terrace-elevation and uplift-rate estimates plotted in comparison with various parameters (i.e., bathymetry,
 760 trench fill, trench distance, wave height, tidal range, precipitation, and coastal azimuth) that might influence the disparate
 761 characteristics of ~~our~~ the marine terrace distribution revealed by our data set. We projected these parameters, elevations,
 762 and uplift rates [with respect](#) to a S-N-oriented polyline that represents the trench. (A) Terrace-elevation measurements and
 763 most important crustal faults (Veloza et al., 2012; Melnick et al., 2020). This shows the range of altitudes in different regions
 764 along the coast and possible relationships [to-between terrace elevation and](#) crustal faulting. The blue horizontal line
 765 indicates the median elevation (30.1 m). (B) Coastal uplift rates and mean bathymetry (GEBCO Bathymetric Compilation
 766 Group, 2020) of a 150-~~km~~-km-swath west of the trench. The blue horizontal line indicates the median uplift rate (0.22
 767 mm/a). (C) Sediment thickness of trench-fill deposits (red) (Bangs and Cande, 1997) and the distance of the trench from
 768

769 our terrace measurements (orange). Flat-slab segments of the subducting Nazca plate are indicated for central Chile and
770 Peru. (D) Maximum wave heights along the WSAC (light green) and the tidal range (dark green) between highest and
771 lowest astronomical tides (Lorscheid and Rovere, 2019). (E) Precipitation (blue) along the WSAC (Ceccherini et al., 2015)
772 and azimuthal orientation of the coastline (cyan). (F) Histogram of terrace-elevation measurements along the WSAC.

773 6. Conclusions

774 We measured 1,953 shoreline-angle elevations as proxies for paleo-sea levels of the MIS-5e and 5c terraces along
775 ~5,000 km of the WSAC between Ecuador and Southern Chile. Our measurements are based on a systematic
776 methodology and the resulting data have been standardized within the framework of the WALIS database. Our
777 mapping was tied using referencing points based on previously published terrace-elevation estimates and age
778 constraints that are summarized in the compilation of Pedoja et al. (2011). The limitations of this database are
779 associated with the temporal accuracy and spatial distribution of the referencing points, which we attempt to consider
780 by providing a ~~quality-quality~~-rating value to each measurement. The marine terrace elevations display a median value
781 of 30.1 m for the MIS-5e level and a median uplift rate of 0.22 m/ka for MIS-5e and 5c. The lowest terrace elevations
782 and uplift rates along the entire South American margin-WSAC occur immediately north of Concepción in Chile (6
783 m, 0.03 m/ka), south of Chiclayo in northern Peru, and on the Santa Elena Peninsula in Ecuador (both 12 m, 0.07
784 m/ka). The regions with exceptionally high marine terrace elevations (≥ 100 m) comprise the Manta Peninsula in
785 Ecuador, the San Juan de Marcona area in south-central Peru, and three regions in south-central Chile (Topocalma,
786 Carranza, and Arauco).

787 The pattern of terrace elevations displays short-, medium- and long-wavelength structures controlled by a combination
788 of various mechanisms. Long-wavelength structures may be controlled by deep-seated processes at the plate interface,
789 such as the subduction of major bathymetric anomalies (e.g. Manta Peninsula and San Juan de Marcona region). In
790 contrast, short- and medium-wavelength deformation patterns may be controlled by crustal faults rooted within the
791 upper plate (e.g., between Mejillones and Valparaíso).

792 Latitudinal climate characteristics along the WSAC may influence the generation and preservation of marine terraces.
793 An increase in wave height and tidal range generally results in enhanced erosion and morphologically well-expressed,
794 sharply defined marine terraces, which correlates with the southward increase in the number of our marine terrace
795 measurements. Conversely, river incision and lateral scouring in areas with high precipitation may degrade marine
796 terraces, thus decreasing the number of potential marine terrace measurements, such as observed south of Valparaíso.

797
798 *Data availability.* The South American database of last interglacial shoreline-angle elevations is available online at
799 <http://doi.org/10.5281/zenodo.4309748> (Freisleben et al., 2020). The description of the WALIS-database fields can
800 be found at <https://doi.org/10.5281/zenodo.3961543> (Rovere et al., 2020).

801
802 *Author contributions.* The main compilers of the database were R.F., J.M.M., and J.J. The paper was written by R.F.
803 with significant input from J.J., D.M., M.S. regarding interpretation and further improvements of graphical data
804 representation.

805
806 *Acknowledgments.* We thank Alessio Rovere for his assistance with the WALIS database. The WALIS database was
807 developed by the ERC Starting Grant "Warmcoasts" (ERC-StG-802414) and PALSEA. PALSEA is a working group
808 of the International Union for Quaternary Sciences (INQUA) and Past Global Changes (PAGES), which in turn

809 received support from the Swiss Academy of Sciences and the Chinese Academy of Sciences. The structure of the
810 database was designed by A. Rovere, D. Ryan, T. Lorscheid, A. Dutton, P. Chutcharavan, D. Brill, N. Jankowski, D.
811 Mueller, M. Bartz, E.J. Gowan and K. Cohen. This study was supported by the Millennium Scientific Initiative of the
812 Chilean government through grant NC160025 “Millennium Nucleus CYCLO The Seismic Cycle Along Subduction
813 Zones”, Chilean National Fund for Development of Science and Technology (FONDECYT) grants 1181479 and
814 1190258, the ANID PIA Anillo ACT192169. R.F. was supported by a research grant of Deutsche
815 Forschungsgemeinschaft to M.S. (DFG STR373/41-1). [Constructive reviews by V. Regard and P.M. Figueiredo](#)
816 [helped to improve the paper.](#)

817

818 7. References

- 819 Anderson, R.S., Densmore, A.L., Ellis, M.A., 1999. The generation and degradation of marine terraces. *Basin*
820 *Research* 11(1), 7–19. doi:10.1046/j.1365-2117.1999.00085.x.
- 821 Angermann, D., Klotz, J., Reigber, C., 1999. Space-geodetic estimation of the Nazca-South America Euler vector.
822 *Earth and Planetary Science Letters* 171(3), 329–334. doi:10.1016/S0012-821X(99)00173-9.
- 823 Baker, A., Allmendinger, R.W., Owen, L.A., Rech, J.A., 2013. Permanent deformation caused by subduction
824 earthquakes in northern Chile. *Nature Geoscience* 6(6), 492–496. doi:10.1038/ngeo1789.
- 825 Bangs, N.L., Cande, S.C., 1997. Episodic development of a convergent margin inferred from structures and
826 processes along the southern Chile margin. *Tectonics* 16(3), 489–503.
- 827 Barazangi, M., Isacks, B.L., 1976. Spatial distribution of earthquakes and subduction of the Nazca plate beneath
828 South America. *Geology* 4(11), 686. doi:10.1130/0091-7613(1976)4<686:SDOEAS>2.0.CO;2.
- 829 Beck, S., Barrientos, S., Kausel, E., Reyes, M., 1998. Source characteristics of historic earthquakes along the central
830 Chile subduction zone. *Journal of South American Earth Sciences* 11(2), 115–129. doi:10.1016/S0895-
831 9811(98)00005-4.
- 832 Bendix, J., Rollenbeck, R., Reudenbach, C., 2006. Diurnal patterns of rainfall in a tropical Andean valley of
833 southern Ecuador as seen by a vertically pointing K-band Doppler radar. *International Journal of Climatology*
834 26(6), 829–846. doi:10.1002/joc.1267.
- 835 Bernhardt, A., Hebbeln, D., Regenberg, M., Lückge, A., Strecker, M.R., 2016. Shelfal sediment transport by an
836 undercurrent forces turbidity-current activity during high sea level along the Chile continental margin. *Geology*
837 44(4), 295–298. doi:10.1130/G37594.1.
- 838 Bernhardt, A., Schwanghart, W., Hebbeln, D., Stuut, J.-B.W., Strecker, M.R., 2017. Immediate propagation of
839 deglacial environmental change to deep-marine turbidite systems along the Chile convergent margin. *Earth and*
840 *Planetary Science Letters* 473, 190–204. doi:10.1016/j.epsl.2017.05.017.

841 Bilek, S.L., 2010. Invited review paper: Seismicity along the South American subduction zone: Review of large
842 earthquakes, tsunamis, and subduction zone complexity. *Tectonophysics* 495(1-2), 2–14.
843 doi:10.1016/j.tecto.2009.02.037.

844 Bilek, S.L., Schwartz, S.Y., DeShon, H.R., 2003. Control of seafloor roughness on earthquake rupture behavior.
845 *Tectonics* 31(5), 455. doi:10.1130/0091-7613(2003)031<0455:COSROE>2.0.CO;2.

846 Binnie, A., Dunai, T.J., Binnie, S.A., Victor, P., González, G., Bolten, A., 2016. Accelerated late quaternary uplift
847 revealed by 10Be exposure dating of marine terraces, Mejillones Peninsula, northern Chile. *Quaternary*
848 *Geochronology* 36, 12–27. doi:10.1016/j.quageo.2016.06.005.

849 Bookhagen, B., Strecker, M.R., 2008. Orographic barriers, high-resolution TRMM rainfall, and relief variations
850 along the eastern Andes. *Geophysical Research Letters* 35(6), 139. doi:10.1029/2007GL032011.

851 Cahill, T., Isacks, B.L., 1992. Seismicity and shape of the subducted Nazca Plate. *Journal of Geophysical Research*
852 97(B12), 17503. doi:10.1029/92JB00493.

853 Ceccherini, G., Ameztoy, I., Hernández, C., Moreno, C., 2015. High-Resolution Precipitation Datasets in South
854 America and West Africa based on Satellite-Derived Rainfall, Enhanced Vegetation Index and Digital Elevation
855 Model. *Remote Sensing* 7(5), 6454–6488. doi:10.3390/rs70506454.

856 Cembrano, J., Lavenu, A., Yañez, G., Riquelme, R., García, M., González, G., Hérial, G., 2007. Neotectonics. In:
857 Moreno, T., Gibbons, W. (Eds.), *The geology of Chile*. Geological Society, London, pp. 231–261.

858 Clift, P., Vannucchi, P., 2004. Controls on tectonic accretion versus erosion in subduction zones: Implications for
859 the origin and recycling of the continental crust. *Reviews of Geophysics* 42(2), 19. doi:10.1029/2003RG000127.

860 Clift, P.D., Hartley, A.J., 2007. Slow rates of subduction erosion and coastal underplating along the Andean margin
861 of Chile and Peru. *Geology* 35(6), 503. doi:10.1130/G23584A.1.

862 Cloos, M., Shreve, R.L., 1988. Subduction-channel model of prism accretion, melange formation, sediment
863 subduction, and subduction erosion at convergent plate margins: 1. Background and description. *Pure and*
864 *Applied Geophysics* 128(3-4), 455–500. doi:10.1007/BF00874548.

865 Cloos, M., Shreve, R.L., 1996. Shear-zone thickness and the seismicity of Chilean- and Marianas-type subduction
866 zones. *Geology* 24(2), 107. doi:10.1130/0091-7613(1996)024<0107:SZTATS>2.3.CO;2.

867 Collot, J.-Y., Charvis, P., Gutscher, M.-A., Operto, S., 2002. Exploring the Ecuador-Colombia Active Margin and
868 Interplate Seismogenic Zone. *Eos, Transactions, American Geophysical Union* 83(17), 185.
869 doi:10.1029/2002EO000120.

870 Collot, J.-Y., Sanclemente, E., Nocquet, J.-M., Leprêtre, A., Ribodetti, A., Jarrin, P., Chlieh, M., Graindorge, D.,
871 Charvis, P., 2017. Subducted oceanic relief locks the shallow megathrust in central Ecuador. *Journal of*
872 *Geophysical Research: Solid Earth* 122(5), 3286–3305. doi:10.1002/2016JB013849.

873 Costa, C., Alvarado, A., Audemard, F., Audin, L., Benavente, C., Bezerra, F.H., Cembrano, J., González, G., López,
874 M., Minaya, E., Santibañez, I., Garcia, J., Arcila, M., Pagani, M., Pérez, I., Delgado, F., Paolini, M., Garro, H.,
875 2020. Hazardous faults of South America; compilation and overview. *Journal of South American Earth Sciences*
876 104(1), 102837. doi:10.1016/j.jsames.2020.102837.

877 Costa, C., Machette, M.N., Dart, R.L., Bastias, H.E., Paredes, J.D., Perucca, L.P., Tello, G.E., Haller, K.M., 2000.
878 Map and database of Quaternary faults and folds in Argentina. Open-File Report. US Geological Survey.
879 <http://dx.doi.org/10.3133/ofr00108>.

880 Coudurier-Curveur, A., Lacassin, R., Armijo, R., 2015. Andean growth and monsoon winds drive landscape
881 evolution at SW margin of South America. *Earth and Planetary Science Letters* 414, 87–99.
882 doi:10.1016/j.epsl.2014.12.047.

883 DeMets, C., Gordon, R.G., Argus, D.F., 2010. Geologically current plate motions. *Geophysical Journal International*
884 181(1), 1–80. doi:10.1111/j.1365-246X.2009.04491.x.

885 Espurt, N., Funicello, F., Martinod, J., Guillaume, B., Regard, V., Faccenna, C., Brusset, S., 2008. Flat subduction
886 dynamics and deformation of the South American plate: Insights from analog modeling. *Tectonics* 27(3), n/a-
887 n/a. doi:10.1029/2007TC002175.

888 Freisleben, R., Jara-Muñoz, J., Melnick, D., Martínez, J.M., Strecker, M., 2020. Marine terraces of the last
889 interglacial period along the Pacific coast of South America (1°N-40°S). Zenodo.
890 doi:10.5281/ZENODO.4309748.

891 Fryer, P., Smoot, N.C., 1985. Processes of seamount subduction in the Mariana and Izu-Bonin trenches. *Marine*
892 *Geology* 64(1-2), 77–90. doi:10.1016/0025-3227(85)90161-6.

893 Fuenzalida, H., Cooke, R., Paskoff, R., Segerstrom, K., Weischet, W., 1965. High Stands of Quaternary Sea Level
894 Along the Chilean Coast. *Geological Society of America Special Papers* 84, 473–496.

895 Gallen, S.F., Wegmann, K.W., Bohnenstiehl, D.R., Pazzaglia, F.J., Brandon, M.T., Fassoulas, C., 2014. Active
896 simultaneous uplift and margin-normal extension in a forearc high, Crete, Greece. *Earth and Planetary Science*
897 *Letters* 398, 11–24. doi:10.1016/j.epsl.2014.04.038.

898 Gardner, T.W., Fisher, D.M., Morell, K.D., Cupper, M.L., 2013. Upper-plate deformation in response to flat slab
899 subduction inboard of the aseismic Cocos Ridge, Osa Peninsula, Costa Rica. *Lithosphere* 5(3), 247–264.
900 doi:10.1130/L251.1.

901 Garreaud, R.D., 2009. The Andes climate and weather. *Advances in Geosciences* 22, 3–11. doi:10.5194/adgeo-22-3-
902 2009.

903 GEBCO Bathymetric Compilation Group, 2020. The GEBCO_2020 Grid - a continuous terrain model of the global
904 oceans and land. British Oceanographic Data Centre, National Oceanography Centre, NERC, UK.

- 905 Geersen, J., Ranero, C.R., Barckhausen, U., Reichert, C., 2015. Subducting seamounts control interplate coupling
906 and seismic rupture in the 2014 Iquique earthquake area. *Nature communications* 6, 8267.
907 doi:10.1038/ncomms9267.
- 908 German Aerospace Center (DLR), 2018. TanDEM-X - Digital Elevation Model (DEM) - Global, 12m.
- 909 González, G., Carrizo, D., 2003. Segmentación, cinemática y cronología relativa de la deformación tardía de la Falla
910 Salar del Carmen, Sistema de Fallas de Atacama, (23°40'S), norte de Chile. *Revista Geológica de Chile* 30(2).
911 doi:10.4067/S0716-02082003000200005.
- 912 Goy, J.L., Macharé, J., Ortlieb, L., Zazo, C., 1992. Quaternary shorelines in Southern Peru a record of global sea-
913 level fluctuations and tectonic uplift in Chala Bay. *Quaternary International* 15-16, 99–112.
- 914 Gutscher, M.-A., Malavieille, J., Lallemand, S., Collot, J.-Y., 1999. Tectonic segmentation of the North Andean
915 margin: impact of the Carnegie Ridge collision. *Earth and Planetary Science Letters* 168(3-4), 255–270.
916 doi:10.1016/S0012-821X(99)00060-6.
- 917 Gutscher, M.-A., Spakman, W., Bijwaard, H., Engdahl, E.R., 2000. Geodynamics of flat subduction: Seismicity and
918 tomographic constraints from the Andean margin. *Tectonics* 19(5), 814–833. doi:10.1029/1999TC001152.
- 919 Hampel, A., 2002. The migration history of the Nazca Ridge along the Peruvian active margin: a re-evaluation.
920 *Earth and Planetary Science Letters* 203(2), 665–679. doi:10.1016/S0012-821X(02)00859-2.
- 921 Hayes, G.P., Moore, G.L., Portner, D.E., Hearne, M., Flamme, H., Furtney, M., Smoczyk, G.M., 2018. Slab2, a
922 comprehensive subduction zone geometry model. *Science (New York, N.Y.)* 362(6410), 58–61.
923 doi:10.1126/science.aat4723.
- 924 Hearty, P.J., Hollin, J.T., Neumann, A.C., O’Leary, M.J., McCulloch, M., 2007. Global sea-level fluctuations during
925 the Last Interglaciation (MIS 5e). *Quaternary Science Reviews* 26(17-18), 2090–2112.
926 doi:10.1016/j.quascirev.2007.06.019.
- 927 Hilde, T.W.C., 1983. Sediment subduction versus accretion around the Pacific. *Tectonophysics* 99(2-4), 381–397.
928 doi:10.1016/0040-1951(83)90114-2.
- 929 Houston, J., Hartley, A.J., 2003. The central Andean west-slope rainshadow and its potential contribution to the
930 origin of hyper-aridity in the Atacama Desert. *International Journal of Climatology* 23(12), 1453–1464.
931 doi:10.1002/joc.938.
- 932 Hsu, J.T., 1992. Quaternary uplift of the Peruvian coast related to the subduction of the Nazca Ridge: 13.5 to 15.6
933 degrees south latitude. *Quaternary International* 15-16, 87–97. doi:10.1016/1040-6182(92)90038-4.
- 934 Hsu, J.T., Leonard, E.M., Wehmiller, J.F., 1989. Aminostratigraphy of Peruvian and Chilean Quaternary marine
935 terraces. *Quaternary Science Reviews* 8(3), 255–262. doi:10.1016/0277-3791(89)90040-1.

- 936 Huene, R. von, Pecher, I.A., Gutscher, M.-A., 1996. Development of the accretionary prism along Peru and material
937 flux after subduction of Nazca Ridge. *Tectonics* 15(1), 19–33. doi:10.1029/95TC02618.
- 938 Jaillard, E., Hérail, G., Monfret, T., Díaz-Martínez, E., Baby, P., Lavenu, A., Dumont, J.F., 2000. Tectonic evolution
939 of the Andes of Ecuador, Peru, Bolivia, and northernmost Chile. In: Cordani, U.G., Milani, E.J., Thomaz, F.A.,
940 Campos, D.A. (Eds.), *Tectonic evolution of South America*. Sociedade Brasileira de Geologia, Rio de Janeiro,
941 pp. 481–559.
- 942 Jara-Muñoz, J., Melnick, D., Brill, D., Strecker, M.R., 2015. Segmentation of the 2010 Maule Chile earthquake
943 rupture from a joint analysis of uplifted marine terraces and seismic-cycle deformation patterns. *Quaternary*
944 *Science Reviews* 113, 171–192. doi:10.1016/j.quascirev.2015.01.005.
- 945 Jara-Muñoz, J., Melnick, D., Socquet, A., Cortés-Aranda, J., Strecker, M.R., 2018. Slip rate and earthquake
946 recurrence of the Pichilemu Fault. *Congreso Geológico Chileno*, 15th.
- 947 Jara-Muñoz, J., Melnick, D., Strecker, M.R., 2016. TerraceM: A MATLAB® tool to analyze marine and lacustrine
948 terraces using high-resolution topography. *Geosphere* 12(1), 176–195. doi:10.1130/GES01208.1.
- 949 Jara-Muñoz, J., Melnick, D., Zambrano, P., Rietbrock, A., González, J., Argandoña, B., Strecker, M.R., 2017.
950 Quantifying offshore fore-arc deformation and splay-fault slip using drowned Pleistocene shorelines, Arauco
951 Bay, Chile. *Journal of Geophysical Research: Solid Earth* 122(6), 4529–4558. doi:10.1002/2016JB013339.
- 952 Jordan, T.E., Isacks, B.L., Allmendinger, R.W., Brewer, J.A.O.N., Ramos, V.A., Ando, C.J., 1983. Andean tectonics
953 related to geometry of subducted Nazca plate. *Geological Society of America Bulletin* 94(3), 341.
954 doi:10.1130/0016-7606(1983)94<341:ATRTGO>2.0.CO;2.
- 955 Kay, S.M., Maksiyev, V., Moscoso, R., Mpodozis, C., Nasi, C., 1987. Probing the evolving Andean Lithosphere:
956 Mid-Late Tertiary magmatism in Chile (29°–30°30'S) over the modern zone of subhorizontal subduction.
957 *Journal of Geophysical Research* 92(B7), 6173. doi:10.1029/JB092iB07p06173.
- 958 Lajoie, K.R., 1986. Coastal tectonics. In: Wallace, R.E. (Ed.), *Active tectonics*. National Academics Press,
959 Washington D.C., pp. 95–124.
- 960 Lamb, S., Davis, P., 2003. Cenozoic climate change as a possible cause for the rise of the Andes. *Nature* 425(6960),
961 792–797. doi:10.1038/nature02049.
- 962 Lohrmann, J., Kukowski, N., Adam, J., Oncken, O., 2003. The impact of analogue material properties on the
963 geometry, kinematics, and dynamics of convergent sand wedges. *Journal of Structural Geology* 25(10), 1691–
964 1711. doi:10.1016/S0191-8141(03)00005-1.
- 965 Lorscheid, T., Rovere, A., 2019. The indicative meaning calculator – quantification of paleo sea-level relationships
966 by using global wave and tide datasets. *Open Geospatial Data, Software and Standards* 4(1), 591.
967 doi:10.1186/s40965-019-0069-8.

968 Macharé, J., Ortlieb, L., 1992. Plio-Quaternary vertical motions and the subduction of the Nazca Ridge, central coast
969 of Peru. *Tectonophysics* 205(1-3), 97–108. doi:10.1016/0040-1951(92)90420-B.

970 Maldonado, V., Contreras, M., Melnick, D., 2021. A comprehensive database of active and potentially-active
971 continental faults in Chile at 1:25,000 scale. *Scientific data* 8(1), 20. doi:10.1038/s41597-021-00802-4.

972 Manea, V.C., Pérez-Gussinyé, M., Manea, M., 2012. Chilean flat slab subduction controlled by overriding plate
973 thickness and trench rollback. *Geology* 40(1), 35–38. doi:10.1130/G32543.1.

974 Mann, P., Taylor, F.W., Lagoe, M.B., Quarles, A., Burr, G., 1998. Accelerating late Quaternary uplift of the New
975 Georgia Island Group (Solomon island arc) in response to subduction of the recently active Woodlark spreading
976 center and Coleman seamount. *Tectonophysics* 295(3-4), 259–306. doi:10.1016/S0040-1951(98)00129-2.

977 Marcaillou, B., Collot, J.-Y., Ribodetti, A., d'Acremont, E., Mahamat, A.-A., Alvarado, A., 2016. Seamount
978 subduction at the North-Ecuadorian convergent margin: Effects on structures, inter-seismic coupling and
979 seismogenesis. *Earth and Planetary Science Letters* 433, 146–158. doi:10.1016/j.epsl.2015.10.043.

980 Martinod, J., Regard, V., Letourmy, Y., Henry, H., Hassani, R., Baratchart, S., Carretier, S., 2016a. How do
981 subduction processes contribute to forearc Andean uplift? Insights from numerical models. *Journal of*
982 *Geodynamics* 96, 6–18. doi:10.1016/j.jog.2015.04.001.

983 Martinod, J., Regard, V., Riquelme, R., Aguilar, G., Guillaume, B., Carretier, S., Cortés-Aranda, J., Leanni, L.,
984 Hérail, G., 2016b. Pleistocene uplift, climate and morphological segmentation of the Northern Chile coasts
985 (24°S–32°S): Insights from cosmogenic ¹⁰Be dating of paleoshorelines. *Geomorphology* 274, 78–91.
986 doi:10.1016/j.geomorph.2016.09.010.

987 Melet, A., Teatini, P., Le Cozannet, G., Jamet, C., Conversi, A., Benveniste, J., Almar, R., 2020. Earth Observations
988 for Monitoring Marine Coastal Hazards and Their Drivers. *Surveys in Geophysics* 41(6), 1489–1534.
989 doi:10.1007/s10712-020-09594-5.

990 Melnick, D., 2016. Rise of the central Andean coast by earthquakes straddling the Moho. *Nature Geoscience* 9(5),
991 401–407. doi:10.1038/ngeo2683.

992 Melnick, D., Bookhagen, B., Echtler, H.P., Strecker, M.R., 2006. Coastal deformation and great subduction
993 earthquakes, Isla Santa Maria, Chile (37°S). *Geological Society of America Bulletin* 118(11-12), 1463–1480.
994 doi:10.1130/B25865.1.

995 Melnick, D., Bookhagen, B., Strecker, M.R., Echtler, H.P., 2009. Segmentation of megathrust rupture zones from
996 fore-arc deformation patterns over hundreds to millions of years, Arauco peninsula, Chile. *Journal of*
997 *Geophysical Research: Solid Earth* 114(B1), 6140. doi:10.1029/2008JB005788.

998 Melnick, D., Hillemann, C., Jara-Muñoz, J., Garrett, E., Cortés-Aranda, J., Molina, D., Tassara, A., Strecker, M.R.,
999 2019. Hidden Holocene slip along the coastal El Yolki Fault in Central Chile and its possible link with

1000 megathrust earthquakes. *Journal of Geophysical Research: Solid Earth* 124(7), 7280–7302.
1001 doi:10.1029/2018JB017188.

1002 Melnick, D., Maldonado, V., Contreras, M., 2020. Database of active and potentially-active continental faults in
1003 Chile at 1:25,000 scale. PANGAEA - Data Publisher for Earth & Environmental Science.
1004 doi:10.1594/PANGAEA.922241.

1005 Melosh, H.J., Raefsky, A., 1980. The dynamical origin of subduction zone topography. *Geophysical Journal*
1006 *International* 60(3), 333–354. doi:10.1111/j.1365-246X.1980.tb04812.x.

1007 Menant, A., Angiboust, S., Gerya, T., Lacassin, R., Simoes, M., Grandin, R., 2020. Transient stripping of
1008 subducting slabs controls periodic forearc uplift. *Nature communications* 11(1), 1823. doi:10.1038/s41467-020-
1009 15580-7.

1010 Morgan, J.K., Bangs, N.L., 2017. Recognizing seamount-forearc collisions at accretionary margins: Insights from
1011 discrete numerical simulations. *Geology* 45(7), 635–638. doi:10.1130/G38923.1.

1012 Müller, R.D., Sdrolias, M., Gaina, C., Roest, W.R., 2008. Age, spreading rates, and spreading asymmetry of the
1013 world's ocean crust. *Geochemistry, Geophysics, Geosystems* 9(4). doi:10.1029/2007GC001743.

1014 Naranjo, J.A., 1987. Interpretacion de la actividad cenozoica superior a lo largo de la Zona de Falla Atacama, Norte
1015 de Chile. *Revista Geológica de Chile*(31), 43–55.

1016 Ortlieb, L., Macharé, J., 1990. Geochronologia y morfoestratigrafia de terrazas marinas del Pleistoceno superior: El
1017 caso de San Juan-Marcona, Peru. *Boletín de la Sociedad Geológica del Perú* 81, 87–106.

1018 Ortlieb, L., Zazo, C., Goy, J., Hillaire-Marcel, C., Ghaleb, B., Cournoyer, L., 1996a. Coastal deformation and sea-
1019 level changes in the northern Chile subduction area (23°S) during the last 330 ky. *Quaternary Science Reviews*
1020 15(8-9), 819–831. doi:10.1016/S0277-3791(96)00066-2.

1021 Ortlieb, L., Zazo, C., Goy, J.L., Dabrio, C., Macharé, J., 1996b. Pampa del Palo: an anomalous composite marine
1022 terrace on the uprising coast of southern Peru. *Journal of South American Earth Sciences* 9(5-6), 367–379.
1023 doi:10.1016/S0895-9811(96)00020-X.

1024 Ota, Y., Miyauchi, T., Paskoff, R., Koba, M., 1995. Plio-Quaternary marine terraces and their deformation along the
1025 Altos de Talinay, North-Central Chile. *Revista Geológica de Chile* 22(1), 89–102.

1026 Paris, P.J., Walsh, J.P., Corbett, D.R., 2016. Where the continent ends. *Geophysical Research Letters* 43(23),
1027 12,208-12,216. doi:10.1002/2016GL071130.

1028 Pedoja, K., Dumont, J.F., Lamothe, M., Ortlieb, L., Collot, J.-Y., Ghaleb, B., Auclair, M., Alvarez, V., Labrousse,
1029 B., 2006a. Plio-Quaternary uplift of the Manta Peninsula and La Plata Island and the subduction of the Carnegie
1030 Ridge, central coast of Ecuador. *Journal of South American Earth Sciences* 22(1-2), 1–21.
1031 doi:10.1016/j.jsames.2006.08.003.

- 1032 Pedoja, K., Husson, L., Regard, V., Cobbold, P.R., Ostanciaux, E., Johnson, M.E., Kershaw, S., Saillard, M.,
1033 Martinod, J., Furgerot, L., Weill, P., Delcaillau, B., 2011. Relative sea-level fall since the last interglacial stage:
1034 Are coasts uplifting worldwide? *Earth-Science Reviews* 108(1-2), 1–15. doi:10.1016/j.earscirev.2011.05.002.
- 1035 Pedoja, K., Ortlieb, L., Dumont, J.F., Lamothe, M., Ghaleb, B., Auclair, M., Labrousse, B., 2006b. Quaternary
1036 coastal uplift along the Talara Arc (Ecuador, Northern Peru) from new marine terrace data. *Marine Geology*
1037 228(1-4), 73–91. doi:10.1016/j.margeo.2006.01.004.
- 1038 Pilger, R.H., 1981. Plate reconstructions, aseismic ridges, and low-angle subduction beneath the Andes. *Geological*
1039 *Society of America Bulletin* 92(7), 448. doi:10.1130/0016-7606(1981)92<448:PRARAL>2.0.CO;2.
- 1040 Prémaillon, M., Regard, V., Dewez, T.J.B., Auda, Y., 2018. GlobR2C2 (Global Recession Rates of Coastal Cliffs): a
1041 global relational database to investigate coastal rocky cliff erosion rate variations. *Earth Surface Dynamics* 6(3),
1042 651–668. doi:10.5194/esurf-6-651-2018.
- 1043 Rabassa, J., Clapperton, C.M., 1990. Quaternary glaciations of the southern Andes. *Quaternary Science Reviews*
1044 9(2-3), 153–174. doi:10.1016/0277-3791(90)90016-4.
- 1045 Ramos, V.A., Folguera, A., 2009. Andean flat-slab subduction through time. *Geological Society, London, Special*
1046 *Publications* 327(1), 31–54. doi:10.1144/SP327.3.
- 1047 Regard, V., Saillard, M., Martinod, J., Audin, L., Carretier, S., Pedoja, K., Riquelme, R., Paredes, P., Hérail, G.,
1048 2010. Renewed uplift of the Central Andes Forearc revealed by coastal evolution during the Quaternary. *Earth*
1049 *and Planetary Science Letters* 297(1-2), 199–210. doi:10.1016/j.epsl.2010.06.020.
- 1050 Rehak, K., Bookhagen, B., Strecker, M.R., Echtler, H.P., 2010. The topographic imprint of a transient climate
1051 episode: the western Andean flank between 15.5° and 41.5°S. *Earth Surface Processes and Landforms* 35(13),
1052 1516–1534. doi:10.1002/esp.1992.
- 1053 Rodríguez, M.P., Carretier, S., Charrier, R., Saillard, M., Regard, V., Hérail, G., Hall, S., Farber, D., Audin, L.,
1054 2013. Geochronology of pediments and marine terraces in north-central Chile and their implications for
1055 Quaternary uplift in the Western Andes. *Geomorphology* 180-181, 33–46.
1056 doi:10.1016/j.geomorph.2012.09.003.
- 1057 Rohling, E.J., Grant, K., Bolshaw, M., Roberts, A.P., Siddall, M., Hemleben, C., Kucera, M., 2009. Antarctic
1058 temperature and global sea level closely coupled over the past five glacial cycles. *Nature Geoscience* 2(7), 500–
1059 504. doi:10.1038/ngeo557.
- 1060 Rovere, A., Ryan, D., Murray-Wallace, C., Simms, A., Vacchi, M., Dutton, A., Lorscheid, T., Chutcharavan, P.,
1061 Brill, D., Bartz, M., Jankowski, N., Mueller, D., Cohen, K., Gowan, E., 2020. Descriptions of database fields for
1062 the World Atlas of Last Interglacial Shorelines (WALIS). Zenodo. doi:10.5281/ZENODO.3961544.

1063 Ruh, J.B., Sallarès, V., Ranero, C.R., Gerya, T., 2016. Crustal deformation dynamics and stress evolution during
1064 seamount subduction: High-resolution 3-D numerical modeling. *Journal of Geophysical Research: Solid Earth*
1065 121(9), 6880–6902. doi:10.1002/2016JB013250.

1066 Saillard, M., 2008. Dynamique du soulèvement côtier Pléistocène des Andes centrales Etude de l'évolution
1067 géomorphologique et datations (10Be) de séquences de terrasses marines (Sud Pérou - Nord Chili), Université
1068 Paul Sabatier, Toulouse.

1069 Saillard, M., Hall, S.R., Audin, L., Farber, D.L., Hérail, G., Martinod, J., Regard, V., Finkel, R.C., Bondoux, F.,
1070 2009. Non-steady long-term uplift rates and Pleistocene marine terrace development along the Andean margin
1071 of Chile (31°S) inferred from 10Be dating. *Earth and Planetary Science Letters* 277(1-2), 50–63.
1072 doi:10.1016/j.epsl.2008.09.039.

1073 Saillard, M., Hall, S.R., Audin, L., Farber, D.L., Regard, V., Hérail, G., 2011. Andean coastal uplift and active
1074 tectonics in southern Peru: 10Be surface exposure dating of differentially uplifted marine terrace sequences (San
1075 Juan de Marcona, ~15.4°S). *Geomorphology* 128(3-4), 178–190. doi:10.1016/j.geomorph.2011.01.004.

1076 Santibáñez, I., Cembrano, J., García-Pérez, T., Costa, C., Yáñez, G., Marquardt, C., Arancibia, G., González, G.,
1077 2019. Crustal faults in the Chilean Andes: geological constraints and seismic potential. *Andean Geology* 46(1),
1078 32. doi:10.5027/andgeoV46n1-3067.

1079 Scholl, D.W., Huene, R. von, 2007. Crustal recycling at modern subduction zones applied to the past—Issues of
1080 growth and preservation of continental basement crust, mantle geochemistry, and supercontinent reconstruction.
1081 In: *4-D Framework of Continental Crust*. Geological Society of America, pp. 9–32.

1082 Schwanghart, W., Kuhn, N.J., 2010. TopoToolbox: A set of Matlab functions for topographic analysis.
1083 *Environmental Modelling & Software* 25(6), 770–781. doi:10.1016/j.envsoft.2009.12.002.

1084 Schweller, W.J., Kulm, L.D., Prince, R.A., 1981. Tectonics, structure, and sedimentary framework of the Peru-Chile
1085 Trench. *Geological Society of America Memoir* 154, 323–350. doi:10.1130/MEM154-p323.

1086 Shackleton, N.J., Sánchez-Goñi, M.F., Pailler, D., Lancelot, Y., 2003. Marine Isotope Substage 5e and the Eemian
1087 Interglacial. *Global and Planetary Change* 36(3), 151–155. doi:10.1016/S0921-8181(02)00181-9.

1088 Shepherd, A., Wingham, D., 2007. Recent sea-level contributions of the Antarctic and Greenland ice sheets. *Science*
1089 (New York, N.Y.) 315(5818), 1529–1532. doi:10.1126/science.1136776.

1090 Siddall, M., Chappell, J., Potter, E.-K., 2006. Eustatic sea level during past interglacials. In: Sirocko, F., Litt, T.,
1091 Claussen, M., Sanchez-Goni, M.-F. (Eds.), *The climate of past interglacials*. Elsevier, Amsterdam, pp. 75–92.

1092 Sobolev, S.V., Babeyko, A.Y., 2005. What drives orogeny in the Andes? *Geology* 33(8), 617–620.
1093 doi:10.1130/G21557AR.1.

- 1094 Stern, C.R., 1991. Role of subduction erosion in the generation of Andean magmas. *Geology* 19(1), 78.
1095 doi:10.1130/0091-7613(1991)019<0078:ROSEIT>2.3.CO;2.
- 1096 Stewart, I.S., Sauber, J., Rose, J., 2000. Glacio-seismotectonics: ice sheets, crustal deformation and seismicity.
1097 *Quaternary Science Reviews* 19(14-15), 1367–1389. doi:10.1016/S0277-3791(00)00094-9.
- 1098 Stirling, C.H., Esat, T.M., Lambeck, K., McCulloch, M.T., 1998. Timing and duration of the Last Interglacial:
1099 evidence for a restricted interval of widespread coral reef growth. *Earth and Planetary Science Letters* 160(3-4),
1100 745–762. doi:10.1016/S0012-821X(98)00125-3.
- 1101 Strecker, M.R., Alonso, R.N., Bookhagen, B., Carrapa, B., Hilley, G.E., Sobel, E.R., Trauth, M.H., 2007. Tectonics
1102 and Climate of the Southern Central Andes. *Annual Review of Earth and Planetary Sciences* 35(1), 747–787.
1103 doi:10.1146/annurev.earth.35.031306.140158.
- 1104 Suárez, G., Molnar, P., Burchfiel, B.C., 1983. Seismicity, fault plane solutions, depth of faulting, and active
1105 tectonics of the Andes of Peru, Ecuador, and southern Colombia. *Journal of Geophysical Research* 88(B12),
1106 10403–10428. doi:10.1029/JB088iB12p10403.
- 1107 Taylor, F.W., Frohlich, C., Lecolle, J., Strecker, M., 1987. Analysis of partially emerged corals and reef terraces in
1108 the central Vanuatu Arc: Comparison of contemporary coseismic and nonseismic with quaternary vertical
1109 movements. *Journal of Geophysical Research* 92(B6), 4905. doi:10.1029/JB092iB06p04905.
- 1110 Trenhaile, A.S., 2002. Modeling the development of marine terraces on tectonically mobile rock coasts. *Marine*
1111 *Geology* 185(3-4), 341–361. doi:10.1016/S0025-3227(02)00187-1.
- 1112 Turcotte, D.L., Schubert, G., 1982. *Geodynamics: Applications of Continuum Physics to Geological Problems*. John
1113 Wiley, New York (450 pp.).
- 1114 Veloza, G., Styron, R., Taylor, M., Mora, A., 2012. Open-source archive of active faults for northwest South
1115 America. *GSA Today* 22(10), 4–10. doi:10.1130/GSAT-G156A.1.
- 1116 Venzke, E., 2013. *Volcanoes of the World*, v. 4.3.4. Global Volcanism Program.
- 1117 Victor, P., Sobiesiak, M., Glodny, J., Nielsen, S.N., Oncken, O., 2011. Long-term persistence of subduction
1118 earthquake segment boundaries: Evidence from Mejillones Peninsula, northern Chile. *Journal of Geophysical*
1119 *Research* 116(B2), 93. doi:10.1029/2010JB007771.
- 1120 Villegas-Lanza, J.C., Chlieh, M., Cavalié, O., Tavera, H., Baby, P., Chire-Chira, J., Nocquet, J.-M., 2016. Active
1121 tectonics of Peru: Heterogeneous interseismic coupling along the Nazca megathrust, rigid motion of the
1122 Peruvian Sliver, and Subandean shortening accommodation. *Journal of Geophysical Research: Solid Earth*
1123 121(10), 7371–7394. doi:10.1002/2016JB013080.

- 1124 von Huene, R., Corvalán, J., Flueh, E.R., Hinz, K., Korstgard, J., Ranero, C.R., Weinrebe, W., 1997. Tectonic
1125 control of the subducting Juan Fernández Ridge on the Andean margin near Valparaiso, Chile. *Tectonics* 16(3),
1126 474–488. doi:10.1029/96TC03703.
- 1127 von Huene, R., Scholl, D.W., 1991. Observations at convergent margins concerning sediment subduction,
1128 subduction erosion, and the growth of continental crust. *Geology* 29(3), 279. doi:10.1029/91RG00969.
- 1129 Wang, K., Bilek, S.L., 2011. Do subducting seamounts generate or stop large earthquakes? *Geology* 39(9), 819–822.
1130 doi:10.1130/G31856.1.
- 1131 Wang, K., Bilek, S.L., 2014. Invited review paper: Fault creep caused by subduction of rough seafloor relief.
1132 *Tectonophysics* 610, 1–24. doi:10.1016/j.tecto.2013.11.024.
- 1133 Watts, A.B., Daly, S.F., 1981. Long Wavelength Gravity and Topography Anomalies. *Annual Review of Earth and*
1134 *Planetary Sciences* 9, 415–448.